Charles University in Prague
Faculty of Science

Study programme: Chemistry

Branch of study: Physical chemistry

Bc. Veronika Sutrová

OPTIMIZATION OF NEW ACTIVE SURFACES BASED ON PLASMONIC NANOPARTICLE ASSEMBLIES FOR SERS, SERRS AND SURFACE-MODIFIED LUMINESCENCE STUDIES OF SELECTED MOLECULES

Optimalizace nových aktivních povrchů tvořených soubory plasmonických nanočástic pro studium SERS, SERRS a povrchem modifikované luminiscence vybraných molekul

Diploma thesis

Supervisor: Prof. RNDr. Blanka Vlčková, CSc.
Consultant: RNDr. Ivana Šloufová, PhD.

Prague, 2015

Abstract

Two types of 3-dimensional (3D) Ag nanosponge aggregates were prepared and tested as samples for surface-enhanced Raman scattering (SERS) and as active surfaces for surface-enhanced luminescence. 3D Ag nanosponge aggregates were assembled from 2D fused fractal aggregates (D = 1.87 ± 0.02) prepared by modification of Ag nanoparticle (NP) hydrosol resulting from the reduction of $AgNO_3$ by $NH_2OH{\cdot}HCl$. For SERS measurements, 3D Ag nanosponge aggregates with incorporated $[Ru(bpy)_3]^{2+}$ cations and chloride anions were prepared and overlayed by a thin layer of aqueous phase. For SEL measurements, the 3D Ag nanosponge aggregates were assembled from fused fractal aggregates of chloride-modified Ag NPs. After preparation the active surface was overlayed by a 1×10^{-5} M aqueous solution of $[Ru(bpy)_3]^{2+}$.

The SERRS (1×10^{-15} M) and SER(R)S (1×10^{-14} M) limits of detection of $[Ru(bpy)_3]^{2+}$ determined at 445 and 532 nm excitations, respectively, correspond to the single molecule level of the complex detection. Its achievement is attributed to a large electromagnetic mechanism enhancement experienced by $[Ru(bpy)_3]^{2+}$ incorporated in "hot spots", an efficient localization of "hot spots" in the 3D aggregate to the focus of the laser beam in micro-Raman spectral measurements and to a molecular resonance contribution to the overall enhancement. Another benefit for SERS spectral measurements from the 3D Ag nanosponge aggregate is protection of the analyte (i.e. $[Ru(bpy)_3]^{2+}$) against thermal decomposition by the thin aqueous phase overlayer.

Phosphorescence measurements from 3D Ag nanosponge aggregate overlayed by 1×10^{-5} M aqueous solution of $[Ru(bpy)_3]^{2+}$ have shown enhancement of fluorescence intensity by factor of 70. The phosphorescence lifetime imaging microscopy (PLIM) measurement yielded three different lifetimes. The 367 ns lifetime belongs to free $[Ru(bpy)_3]^{2+}$, while the other two lifetimes – 75 and 17 ns are attributed to $[Ru(bpy)_3]^{2+}$ cations localized in the vicinity of the aggregate or in the aggregate pores.

2D arrays of co-assembled hydrophobic Au NPs and SQDs were prepared from their organosols in toluene at water surface in various weight ratios. The 1:1, 1:2 and 2:1 ratios were found to be optimal for semiregular 2D co-assembling of Au NPs and SQDs. In these assemblies, localization of SQDs between Au NPs led to enhancement of the SQDs fluorescence by the factor of 7 – 8.

Keywords: plasmonic nanoparticles, SERS, SERRS, surface-modified luminescence, semiconductor quantum dots, Ru (II) tris(2,2'-bipyridine)

Abstrakt

Byly připraveny dva typy 3-dimenzionálních (3D) Ag agregátů s vnitřní nanohoubovitou strukturou a testovány jako vzorky pro povrchem zesílený Ramanův rozptyl (SERS) a jako aktivní povrchy pro povrchem zesílenou luminiscencí. 3D Ag agregát s vnitřní nanohoubovitou strukturou byl připraven z fraktálních 2D fúzovaných agregátů (D = 1,87 ± 0,02) získaných modifikací hydrosolu Ag nanočástic (NČ) připraveného redukcí $AgNO_3$ pomocí $NH_2OH{\cdot}HCl$. Pro SERS měření byl připraven Ag agregát se začleněnými kationty $[Ru(bpy)_3]^{2+}$ a Cl^- anionty, který byl převrstven tenkou vrstvou vodné fáze. Modifikací Ag NČ chloridy vznikly fraktální fúzované agregáty, ze kterých byl následně připraven 3D Ag agregát pro měření povrchem zesílené luminiscence. Po přípravě byl agregát převrstven 1×10^{-5} M vodným roztokem $[Ru(bpy)_3]^{2+}$.

SERRS (1×10^{-14} M) a SERS (1×10^{-15} M) limity detekce $[Ru(bpy)_3]^{2+}$ určené při excitační vlnové délce 445 a 532 nm odpovídají mezi detekce na úrovni detekce jedné molekuly. K možnosti detekce na úrovni jedné molekuly přispívá zesílení elektromagnetickým mechanismem v důsledku lokalizace $[Ru(bpy)_3]^{2+}$ do „hot spots“, efektivní lokalizace „hot spots“ do fokusu laserového svazku při mikro-Ramanském spektrálním měření a příspěvek molekulární rezonance k celkovém zesílení signálu.

Fosforescenční měření z 3D Ag agregátu převrstveného vodným roztokem 1×10^{-5} M $[Ru(bpy)_3]^{2+}$ prokázala zesílení intenzity fosforescence faktorem 70. Zároveň z PLIM (Phosphorescence lifetime imaging microscopy) měření byly získány 3 různé doby života excitovaného stavu $[Ru(bpy)_3]^{2+}$. Doba života excitovaného stavu 367 ns odpovídá volnému $[Ru(bpy)_3]^{2+}$, další dva 75 ns a 17 ns odpovídají lokalizaci kationtů $[Ru(bpy)_3]^{2+}$ do blízkosti povrchu Ag agregátu nebo do jeho pórů.

Z toluenových organosolů hydrofobních Au NČ a polovodičových kvantových teček s různými váhovými poměry byly připraveny 2D uspořádané vrstvy, na površích vodné fáze. Poměry 1:1, 1:2 a 2:1 se ukázaly jako nejvýhodnější pro vzájemné uspořádávání Au NČ a kvantových teček. Z těchto uspořádaných 2D struktur vedla lokalizace kvantových teček mezi Au NČ k zesílení intenzity jejich fluorescence faktorem 7 – 8.

Keywords: plasmonické nanočástice, SERS, SERRS, povrchem modifikovaná luminiscence, polovodičové kvantové tečky, kation tris(2,2'-bipyridyl)ruthenatý

Statement

Prohlašuji, že jsem závěrečnou práci zpracovala samostatně a že jsem uvedla všechny použité informační zdroje a literaturu. Tato práce ani její podstatná část nebyla předložena k získání jiného nebo stejného akademického titulu.

V Praze, 7. 5. 2015

Podpis

Acknowledgment

I would like to thank my supervisor Prof. RNDr. Blanka Vlčková, CSc. for her patient guidance of my thesis, helpfulness and valuable advice. Then I would like to thank my consultant RNDr. Ivava Šloufová, Ph.D. for her practical advice, support in the laboratoratory and for help with calculations. I would also like to thank RNDr. Markéta Kokošková for her help with introduction into a fluorescence measurements and for her practical advice. I would like to thank doc. RNDr. Miroslav Šlouf, Ph.D. for giving me an opportunity to fluorescence and electron microscopy measurements. I would also like to thank to RNDr. Sabina Krejčíková, CSc. and Ing. Martina Nevoralová, Ph.D. for their advice, help and introduction to SEM microscopy measurements, and Mrs. Jiřina Hromádková for her advice, help and introduction to TEM microscopy measurements.

Finally, I would like to thank my family for their support during the whole my study.

Content

1. Introduction

Surface-enhanced Raman scattering (SERS) and surface-enhanced resonance Raman scattering (SERRS) are well-known spectro-analytical methods, which utilize enhancement of Raman scattering by plasmonic metal nanostructures, e.g. Ag and Au nanoparticles (NPs) [1 – 8]. On the other hand, surface-modified luminescence (SML) is a relatively new method, which also utilizes interaction of luminophores with plasmonic metal nanostructures [9,10].

In SERS or SERRS, only an amplification of Raman signal is observed [1 – 8]. On the other hand, in SML we can observe amplification or attenuation depending on the localization of molecules with respect to the surface of plasmonic metal nanostructures [9,10]. Investigation of SERS, SERRS and SML processes combines molecular spectroscopy with plasmonics and surface science.

The crucial points in design and preparation of new types of samples for SERS and SERRS is an efficient localization of molecules into "hot spots" (strong optical fields localized into nanometer dimensions) for achievement of very low limits of their spectral detection, and, simultaneously, prevention of the molecules decomposition in the "hot spots".

Design and preparation of samples (and/or active surfaces) for SML is motivated chiefly by an effort to combine the nanostructure morphology and optical responses with the absorption and emission characteristics of the luminophore and its suitable localization with respect to the particular nanostructure for achievement of the luminescence signal amplification.

Combination of SERS, SERRs and SML studies requires selection of a luminescent chromophoric species, such as $[Ru(bpy)_3]^{2+}$. This complex dication is a well known luminophore as well as a chromophore [10], whose resonance Raman scattering (RRS) spectra were assigned by normal coordinate analysis (NCA) [11]. This complex and its derivates are also widely used as luminescence probes and sensitizers in dye-sensitized solar cells [12]. Semiconductor quantum dots (SQDs) represent another type of well known and commercially available luminophores [13]. In this thesis, hydrophobic alloyed ZnCdSeS SQDs were selected as the second type of a testing luminophore.

2. Theoretical part

Surface-enhanced Raman scattering (SERS) is well-known spectro-analytical method, which utilizes enhancement of Raman scattering by plasmonic metal nanoparticles (NPs). Applications of SERS or SERRS (Surface-enhanced Resonance Raman Scatterign) are directed chiefly to qualitative and quantitave chemical analysis, medical research, environmental science and protection, material science, art history and archaeology or SERS and SERRS spectral sensing of various molecular species and surface chemistry [1 – 8]. By SERS and SERRS spectral testing it is possible to achieve a single molecule level of spectral detection [1 – 7,14 – 18] .

Plasmonic NPs are metal (mostly Ag, Au and Cu) NPs, which can focus visible light to nanometer dimensions and function as amplifiers of radiation. The aggregates of these NPs also have this ability [1 – 8,19].

SERS spectroscopy of selected molecules is an appropriate method of testing of new types of surfaces for studies of surface-modified optical processes. SERS spectral testing can provide information about localization of adsorbates or about interaction of adsorbates with surfaces of plasmonic NPs [2, 8,20 – 23].

SERS was first observed by Fleischmann et al. in 1974 [24]. Their work was focused Raman spectral studies of pyridine at a roughened Ag electrode. Spectral intensity was unusually high. Fleischmann thought, that the high intensity is caused only by localization of more molecules of pyridine to the roughened (i.e. enlarged) surface of the electrode. In 1977, van Duyne proved that increasing of Raman signal is caused by the effect of surface-enhanced Raman scattering [25].

In addition to roughened electrodes, hydrosols of metal NPs (Au, Ag, Cu), island films, metal NPs – adsorbate or metal aggregates with internal nanostructure can be used for SERS or SERRS spectral studies [1 – 8,26].

2.1. Surface-enhanced Raman scattering spectroscopy

Surface-enhanced Raman scattering (SERS) spectroscopy is based on a simultaneous interaction of visible radiation with nanostructures of plasmonic metals and with molecules localized on their surfaces [1 – 8,19]. SERS and SERRS is currently a spectro-analytical tool which allows for single-molecule level detection [1 – 8].

SERS and SERRS are based on contribution of two main mechanisms, the electromagnetic mechanism (EM) and the mechanism of molecular resonance.

Explanation of the mechanisms is based on references [1 – 8, 15,16,27,28].

2.1.1. Mechanisms of Surface-enhanced Raman scattering

The overall enhancement factor of Raman scattering G in SERS (or SERRS) is given by ratio of the intensity of SERS signal I_{SERS} and of the intensity of the signal of Raman scattering I_{RS} for the same number of scattered molecules N:

$$G = \frac{I_{(SERS)N}}{I_{(RS)N}}. \tag{2.1}$$

Enhancement of Raman scattering is given first of all by the electromagnetic mechanism which is the principal mechanism of SERS. Under appropriate conditions (vide infra), the mechanism of molecular resonance also contributes to the overall enhancement.

The electromagnetic mechanism occurs when the condition of resonance Mie scattering is satisfied. In that case, conduction electrons within the particle oscillate at the same frequency as the frequency of the incident radiation, which creates an oscillating (and re-radiating) dipole. This process is also called dipolar surface plasmon excitation. The mechanism of molecular resonance occurs when the excitation wavelength is suitable for both the excitation of dipolar surface plasmon and for the molecular resonance.

2.1.1.1. Electromagnetic mechanism

The electromagnetic (EM) mechanism is the basic mechanism of SERS. The enhancement factor by the EM mechanism is in $10^4 – 10^{11}$ range. For explanation of EM mechanism, the model of an isolated, spherical nanoparticle (NP) with size about 5 – 20 nm was chosen (Fig. 1). After irradiation of e.g. a Ag NP by radiation of the wavelength at which the condition of resonant Mie scattering (i.e. the condition of the resonance excitation of surface plasmon) is satisfied, conduction electrons within the particle oscillate with the same frequency as the frequency of incident radiation. This leads to creation of oscillating dipole, also called the dipolar (or localized) surface plasmon.

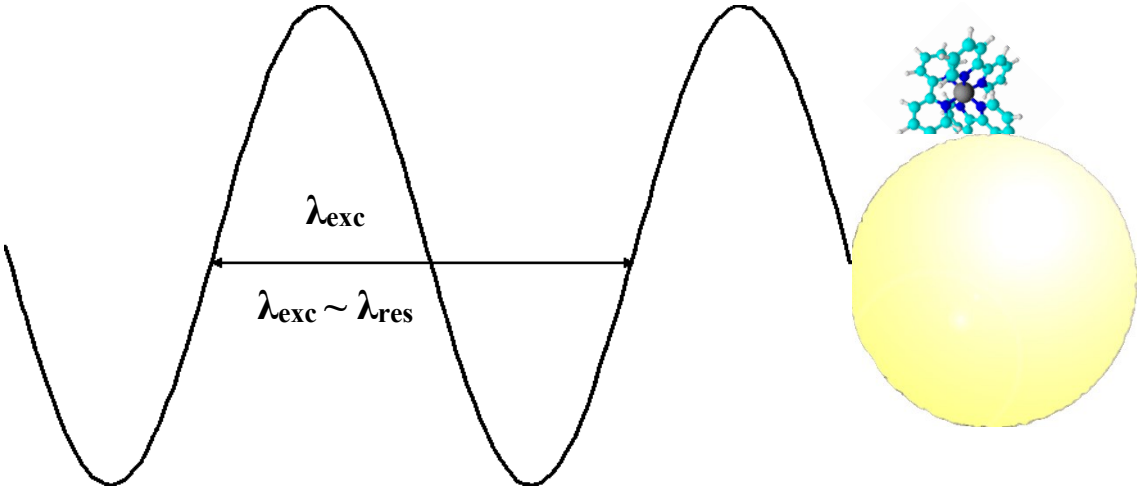

Figure 1: Schematic depiction of model plasmonic NP - molecule

In the quasistatic approximation, the magnitude of the dipole is given by a dipole moment $\vec{P}$:

$$\vec{P} \sim g \cdot r^3 \cdot \overrightarrow{E_0}, \tag{2.2}$$

where $\overrightarrow{E_0}$ is intensity of the incident radiation, r is a radius of the metal sphere and g is the enhancement factor defined as:

$$g = \frac{\varepsilon(\lambda) - \varepsilon_m}{\varepsilon(\lambda) + 2\varepsilon_m}, \tag{2.3}$$

where $\varepsilon(\lambda)$ is a relative complex permittivity (dielectric function) of the metal and ε_m is a relative permittivity (dielectric constant) of the surrounding medium. It is possible to calculate a value of complex permittivity of the metal by formulas:

$$\varepsilon(\lambda) = N^2(\lambda), \tag{2.4}$$

where $N(\lambda)$ is the complex refractive index given by:

$$N(\lambda) = n + ik, \tag{2.5}$$

where n is the refractive index and k is the index of absorption.

The intensity I of radiation, which is produced by the resulting oscillating dipole, is directly proportional to the square of size of the dipole $\vec{P}$:

$$I = \left|\vec{P}\right|^2. \tag{2.6}$$

When the resonant condition is satisfied, intensity of the radiation is maximal. This condition is satisfied, when real component of the complex permittivity is equal to:

$$Re\ \varepsilon(\lambda) = -2\varepsilon_m \tag{2.7}$$

and the imaginary part, which corresponds to the degree of resonance damping, is small:

$$Im\ \varepsilon(\lambda) \to 0. \tag{2.8}$$

This condition is satisfied for the system of isolated NPs with sizes about 5 – 20 nm in water ambient when λ_{exc} = 390 nm for Ag NPs and λ_{exc} = 520 nm for Au NPs. If this condition is satisfied, NPs function as optical amplifiers.

2.1.1.2. Mechanism of molecular resonance

Structure of molecules affects the mechanism of molecular resonance. This mechanism is therefore molecularly specific. Amplification by the mechanism of molecular resonance (MR) is in the 10^2 – 10^3 range. In comparison with the EM mechanism, enhancement by the MR mechanism is significantly weaker.

The mechanism of molecular resonance occurs when the excitation wavelength is suitable for both the excitation of dipolar surface plasmon and for the molecular resonance. Two types of molecular resonance mechanism are recognized – chemical mechanism of SERS and surface-enhancement resonance Raman scattering. The type of MR contribution depends on type of adsorbed molecule. The distinction depends on if this molecule is a chromophore or a nonchromophore with respects to the excitation wavelength.

2.1.1.2.1. Non-Chromophoric molecules – chemical mechanism of SERS

Chemical mechanism of SERS operates, when a metal – adsorbate surface complex is formed, i.e. when the molecule of adsorbate is chemisorbed to the surface of metal NP, and when the resonant condition is satisfied. The resonant condition is satisfied, when the excitation wavelength is suitable for the excitation of the photoinduced charge transfer transition within the newly formed surface complex. Resonant condition must be fulfilled simultaneously with the resonant condition for excitation of surface plasmon.

2.1.1.2.2. Chromophoric molecules – Surface-enhanced resonance Raman scattering

Surface-enhanced resonance Raman scattering (SERRS) occurs, when the excitation wavelength is suitable for fulfilment of resonant condition for excitation of surface plasmon and also for excitation of an allowed electronic transition in the adsorbed molecule. When the geometric and the electronic structure of chromophore after its attachment to the Ag or Au surface is preserved, the molecular resonance condition is satisfied for the same excitation wavelength as in the case of the resonance Raman scattering of the non-adsorbed chromophore.

2.2. Surface modified luminescence

The effect of surface-modified luminescence (SML) was observed, probably for the first time by Drexhage et al in 1970 [29]. He observed changes in lifetimes of excited states of Eu^{3+} depending on distance from the surface of Ag film.

In contrast with SERS, in surface-modified luminescence, attenuation or amplification of luminescence (fluorescence or phosphorescence) can be observed. In evaluation of these processes, coupling from the excited state of the fluorophore to surface plasmons of metallic NPs has to be considered. In particular, by interaction of excited state of the fluorophore with the excited surface plasmon state of the metal NP,

fluorophore – metal exciplex is created. The amplification process is caused chiefly by enhancement of absorption (or emission) of light by fluorophores due to the increased electric fields between and around the metal NPs. In that case, the mechanism of the incident radiation enhancement is similar to that in SERS [9]. Attenuation of luminescence is based on Főrster resonance energy transfer (FRET) [30]. In that case, non-radiative energy transfer from the excited state of the luminescent species to surface plasmon excited state of the metal NP occurs.

Extensive studies have shown that amplification of attenuation of fluorescence depends on distance of fluorophore from the metal NPs surface. A very important study was performed by Novotny et al [31].

Novotny et al [31] studied experimentally and theoretically the effect of distance of the fluorescent sample from a single Au NP. In good agreement with theoretical studies, they measured that the maximal enhancement of fluorescence occurs, when the fluorophore distance from the single Au NP is 5 nm. For shorter distances, fluorescence is quenched. Distance effect of quenching and enhancement of fluorescence is demonstrated in Fig. 2.

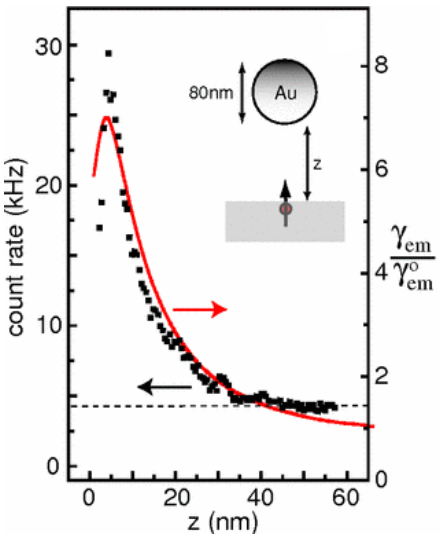

Figure 2: Dependency of fluorescence rate as a function of distance effect of fluorescence from single Au NPs. Adapted from the [31]

Similar distance effect has also been observed by Lakowicz et al and Oates et al [32,33].

The effect of the presence of metal surface on emission of a fluorophore can be explained by Jablonski diagram (Fig. 3).

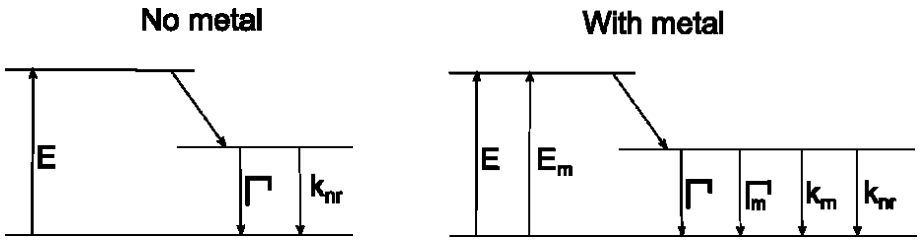

Figure 3: Jablonski diagram without and with metal surface. Γ is radiative decay rate; k_{nr} is non-radiative decay rate; Γ_m is the contribution of the metal presence to the radiative decay rate; k_m is contribution of the metal presence to the non-radiative decay rate; E is excitation rate of a fluorophore in the absence of the metal; E_m is increrase of excitation rate in the presence of the metal.

Quantum yield of fluorescence of fluorophore in the absence of metal surface Φ is given by:

$$\Phi = \frac{\Gamma}{\Gamma + k_{nr}}, \tag{2.9}$$

where Γ is the radiative decay rate and k_{nr} is the non-radiative decay rate. The lifetime of excited state of fluorophore is given by:

$$\tau = \frac{1}{\Gamma + k_{nr}} \tag{2.10}$$

In the presence of metal surface, quantum yield of fluorescence Φ is given by:

$$\Phi = \frac{\Gamma + \Gamma_m}{\Gamma + \Gamma_m + k_{nr}}, \quad (2.11)$$

and lifetime of excited state τ is given by:

$$\tau = \frac{1}{\Gamma + \Gamma_m + k_{nr}}. \quad (2.12)$$

Enhancement factor of metal-enhanced fluorescence as 10^7 [34] was calculated, however enhancement factor 7 – 12 is usually observed [35].

Enhancement factor is most strongly affected by distance effect. However, it was observed, that type and morphology of the metal surface also affects the enhancement of fluorescence. Typical surfaces are metal colloids, rough surfaces, mirrors and metal islands. It was found, that most efficient surfaces for surface-enhanced luminescence (SEL) are colloids and metal islands. Lakowicz et al [30] studied the effect of distance of luminophore from Ag island films. Fuchsin was used as luminophore. They observed amplification of fluorescence at the 4 – 10 nm distance range from surface. The largest amplification was observed when the distance of fuchsin from the surface was 4 nm. Malicka et al [36] studied also effect of distance of fluorophore from Surface island films (SIF), they also observed optimal enhancement in the 5 – 9 nm distance.

2.3. Hydrosols of metal nanoparticles

Hydrosols of metal NPs are the most commonly used surfaces for SERS spectral measurements, especially the hydrosols of Au and Ag NPs. SERS activity of this surface was first mentioned by Moskovits in relation with the theory of EM mechanism in SERS in 1978 [19]. In the same year, Creighton at al [26] experimentally proved this theory. Hydrosols are mostly used for their advantages such as easy preparation, stability for several month or easy instrumentation. Hydrosols of metal NPs could be prepared by laser ablation [37], however they are mostly prepared by chemical reduction of $AgNO_3$ or $HAuCl_4$ by suitable reducing agents [2,4]. Nowadays, it is possible to prepare sols of metal NPs by dissolving of commercially available NPs in a suitable solvent. Ag NPs hydrosols are most commonly used for the suitable dielectric properties of Ag [1 – 4]. The type of the preparation procedure affects chemical properties of hydrosols e.g. concentration of the NPs, surface potential or oxidation state

of adsorption sites at the surface of Ag NPs. Adsorption sites at the surface of Ag NPs affect adsorption of molecules to the surface of Ag NPs [1 – 4,8]. Ag NPs hydrosols contain isolated NPs, which is caused by the formation of an electric double layer enveloping the NPs (Fig. 4). The electric double layer is formed by positively charged Ag^+ ions and negatively charged ions of reduction agent, which was used for preparation (Fig. 4).

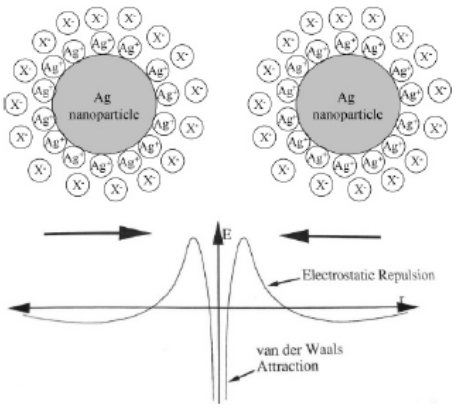

Figure 4: Schematic depiction of isolation of Ag NPs

The largest enhancements of SERS signal are provided by aggregates of metal NPs [1 – 4,8,38]. Aggregation of hydrosol NPs can be caused by addition of a testing adsorbate [39,40] or by a preaggregation agent [22,23]. As preaggregation agent e.g. Cl^- ions can be used [22]. The consequence of NPs aggregation can be most simply explained by the model of the linear aggregate, in which NPs are approximated by identical, nanospheres [27]. When plasmon excitations in spherical NPs interact with each other by dipole-dipole interaction, the original band of plasmon extinction is split into two bands. The first maximum is located close to the maximum of the original excitation band of isolated spheres. On the other hand, the second maximum is red shifted, it means that it is located at higher wavelengths.

The largest amplification of radiation is given by localization of molecules into specific locations of interacting NPs such as dimers or fractal aggregates. In that case, "hot spots" (strong optical fileds localized into nanometer dimensions) are generated after irradiation. In "hot spots", amplification by the EM mechanism is the highest and depends on the morphology of the NP assembly and the excitation wavelength [3,15,16,41]. The enhancement factors up to 10^{11} can be achieved for molecules localized in "hot spots" between closely spaced Ag NPs in dimers [15] (Fig. 5 – B). Fig. 5 demonstrates localization of "hot spots" in fractal aggregates and in plasmonic metal NPs dimers.

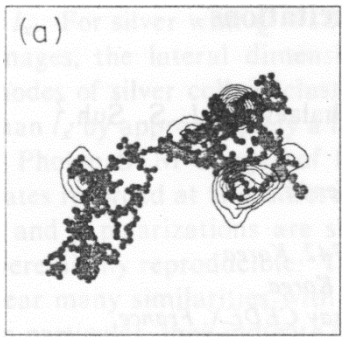

A

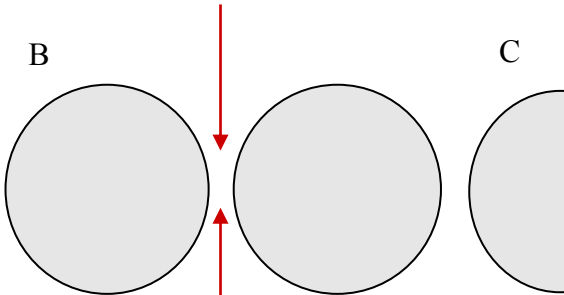

5: Depiction of localization of "hot spots" in (A) fractal aggregates (B) dimer of spaced NPs and (C) intergrown NPs dimer. Adapted from [15,16,28,41]

2.4. Aggregates of metal NPs

Aggregates of metal NPs prepared by modification of metal NPs hydrosol very often contain "hot spot" and thus become suitable as surfaces for SERS spectral testing measurements. The highest benefits of micro-Raman spectral probing of metal NPs aggregates include getting optical images of measurement area and exact localization of laser beam into a sample. Measurements of aggregated metal NPs hydrosol drops performed in micro-Raman spectral setup with immersion objective are suitable, because of protection against thermal decomposition of a testing adsorbate [14].

Micro-Raman spectral testing without immersion objective from "dried" aggregates localized onto a microscopic slide often leads to destruction of samples. For example, spurious bands attributed to thermal decomposition were observed in SERS spectra of 5,10,15,20-tetrakis(1-methyl-4-pyridyl)porphyrin (H_2TMPyP) measured from "dried drops" of Ag NPs aggregates [42]. Thermal decomposition of testing adsorbate leads to formation of spurious bands in spectra.

Recently, 3D nanopores or nanosponge aggregates with internal nanostructure have been reported as prospective active surfaces for SERS. As potentially useful proved to be the metal nanosponge aggregates. These aggregates have shown an internal nanostructure, which retains even in a macroscopic scale. These types of aggregates could be prepared by several ways such as by using of a polymer matrix. In that case, a porous polymer matrix acts as a carrier in which metal NPs are incorporated [43]. Distance between pores may be controlled, on the other hand in SERS spectral measurements signal of used polymer could affect the resulting spectrum of an adsorbate. Meng et al [44] prepared macroscopic metal nanosponge aggregates from pure metals. From these nanosponge aggregates, a disc for macroscopic measurement was prepared. Even the metal disc retained its internal nanosponge structure, enhancement of Raman signal has been too weak. Trindade et al [45] prepared an

aggregate by modification of bacterial cellulose which contained Ag NPs by $MgCl_2$. On the other hand, these aggregates show only microstructural features.

Metal nanosponge aggregates seem to be prospective surfaces for SERS measurement. On the other hand, their preparations reported up to now seem to be too difficult and lengthy, while they do not ensure, that the deposited adsorbate will show a large enhancement of its Raman scattering. Recently, a new pathway to Ag nanosponge aggregates preparation was outlined [46].

2.5. Testing chromophores and luminophores

2.5.1. Tris(bipyridyl) Ru(II) dichloride

Fig. 6 demonstrates the structure of $[Ru(bpy)_3]^{2+}$, which is well known as chromophore and also as luminophore. $[Ru(bpy)_3]^{2+}$ is studied as photocatalyst for splitting of water and it is mainly known for its utilization as sensitizer in dye-sensitized solar cells [12]. $[Ru(bpy)_3]^{2+}$ is also used as testing adsorbate for Raman, RRS, SERS or SERRS spectral testing. An important study by Mallick et al reports resonance Raman and infrared spectra of $[Ru(bpy)_3]^{2+}$ and its deuterated analogues and a normal coordinate analysis (NCA) for $[Ru(bpy)_3]^{2+}$ unit (C_{2v}). A_1 and B_2 fundamental modes were assigned on the basis of NCA [11].

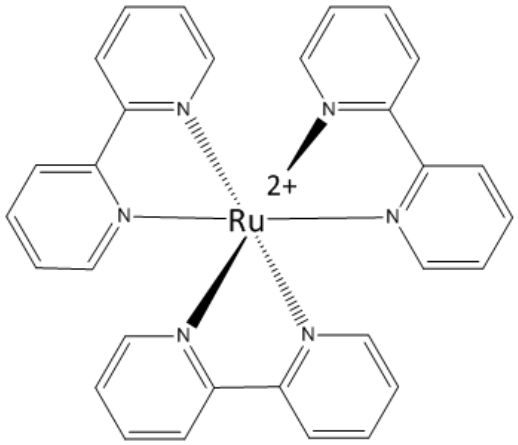

Figure 6: Chemical structure of $[Ru(bpy)_3]^{2+}$

In the study, where Ag NPs hydrosols as active systems and $[Ru(bpy)_3]^{2+}$ and 2,2´-bipyrine as testing adsorbates were used, it was found that the SERRS and SERS spectra of $[Ru(bpy)_3]^{2+}$ are nearly identical with those of Ag(0)-bpy surface complex [22]. The same study was focused also on SERS and SERRS excitation profiles and it was found, that 9 of 10 fundamental bands of both species show a resonance contribution to the overall SERS enhancement. The resonance condition is different for $[Ru(bpy)_3]^{2+}$ and for Ag(0)-bpy surface complex. In the case of $[Ru(bpy)_3]^{2+}$, condition for charge transfer from Ru→(bpy) is satisfied by the excitation wavelengths close to the 453 nm and in the case of Ag(0)-bpy surface complex, condition for charge transfer from Ag(0)→(bpy) is satisfied by the excitation wavelengths close to 540 nm.

Dines et al [47] studied adsorption of $[Ru(bpy)_3]^{2+}$ on the Ag NPs surface in the presence of chlorides, and they determined the limit of the SERS spectral detection as 1×10^{-12} M. They assumed that it was achieved by a combination of resonance enhancement and surface enhancement. They also proved that absorption of $[Ru(bpy)_3]^{2+}$ is governed by a Langmuir adsorption isotherm and they assumed that $[Ru(bpy)_3]^{2+}$ dications are bonded to the negatively charged surface of Ag NPs by an electrostatic bonding. Fig. 7 demonstrates bonding of $[Ru(bpy)_3]^{2+}$ to negatively charged Ag NPs surface.

Chemisorption and electrostatic bonding of Ru(II) polypyridine complexes to Ag NP surfaces were compared for systems with fractal aggregates [23]. Molecular resonance damping of chemisorbed $[Ru(bpy)_2(dcbpy)]^{2+}$ (dcbpy =4,4′-dicarboxy-2,2′-bipyridine) complex was found to be 500x higher than for electrostatically bonded $[Ru(bpy)_3]^{2+}$. The way of adsorption affects the limit of SERS spectral detection (LOD), which in the case of the electrostatically bonded $[Ru(bpy)_3]^{2+}$ was 1×10^{-12} M and for chemisorbed $[Ru(bpy)_2(dcbpy)]^{2+}$ 1×10^{-9} M. It was also found, that electrostatic bonding of chromophoric molecules to negatively charged Ag NPs surface is more advantageous than chemisorption, since the electrostatic bonding to the Ag NPs surface also preserves the native electronic structure of the chromophore [23].

Light absorption of $[Ru(bpy)_3]^{2+}$ occurs in the 400 – 500 nm region. The absorption is attributed to a metal to ligand charge transfer (MLCT) transition from Ru(II) to π* orbital of bpy. The excited state of $[Ru(bpy)_3]^{2+}$ can be written as $[RuIII(bpy)_2(bpy^-)]^{2+}$, in that case Ru(III) is strong oxidant and bpy^- a strong reductant [10,48].
Light emission of $[Ru(bpy)_3]^{2+}$ occurs from the ^{3}MLCT state.

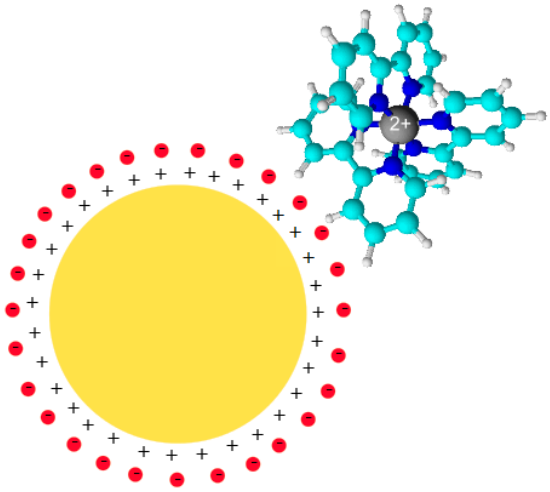

Figure 7: $[Ru(bpy)_3]^{2+}$ electrostatically bonded to negatively charged Ag NP surface

2.5.2. Semiconductor quantum dots

The development of semiconductor quantum dots (SQDs) began in the early 90s of the 20th century [10]. SQDs are in general fluorescent semiconductor nanocrystals, which can exist individually or in clusters. Typical size of SQDs is about 1 – 10 nm. The most typical arrangement is a core-shell structure. In that case one type of semiconductor creates a core (typically CdSe) and the other type of semiconductor creates a shell (typically ZnS) [13]. SQDs have found their use especially in biologically applications, such as in vivo imaging, bioanalysis, drug delivery etc.

SQDs are most often synthesized in non-aqueous solutions. This type of preparation provides the highest quality SQDs. On the other hand, for this type of preparation, toxic precursors are used and also high temperature is necessary. For this reason, synthesis in an aqueous solutions comes to the fore. Both methods are based on preparation of nanocrystals, which are prepared by mixing of suitable precursors and then followed by heating. Another type of preparation of SQDs is based on alloying of materials from which SQDs are prepared [13]. The prepared SQDs can be further modified by various types of polymers or silica, which increase the compatibility with biological materials. Thus modified SQDs can be further labelled with bioaffinity molecules, such as avidin or antibodies [10].

The optical properties of SQDs depend on material which was used and also on size. After absorption of light, an electron – hole pair is created. Recombination of the pair can result in emission of the light. The dependence of the photoluminescence (PL) of SQDs on their size is the result of quantum confinement. With decreasing of the size of bulk material to the nanoscale dimensions, the density of states decreases near to the conduction band and valence band edges, which leads to creation of discrete excitonic states. With decreasing size of nanocrystal, the band gap energy further increases and the exciton (exciton = a bound stateof an electron and a hole which are attracted to each

other by the electrostatic Coulomb force) is confined to smaller dimension than its Bohr radius.

For core-shell SQDs, we distinguish 4 types of SQDs – Type I, Type II, Quasi – Type II and Inverse Type I, which are demonstrated in Fig. 8. The types of SQDs depend on band gap energy between the core and the shell. Type I is a type in which, both the electron and the hole are localized in the core. In a Type II, the electron is localized in the shell and the hole is localized in the core, or vice versa. For a Quasi – Type II is typical a small offset between band edge state of the core and shell and electron is delocalized over whole nanocrystal, however the hole is confined to the core. An Inverse Type I is designed so that both electron and hole are localized into the shell. The size of the band gap or the lattice strain between the core and shell can be used to tune the optical properties of SQDs.

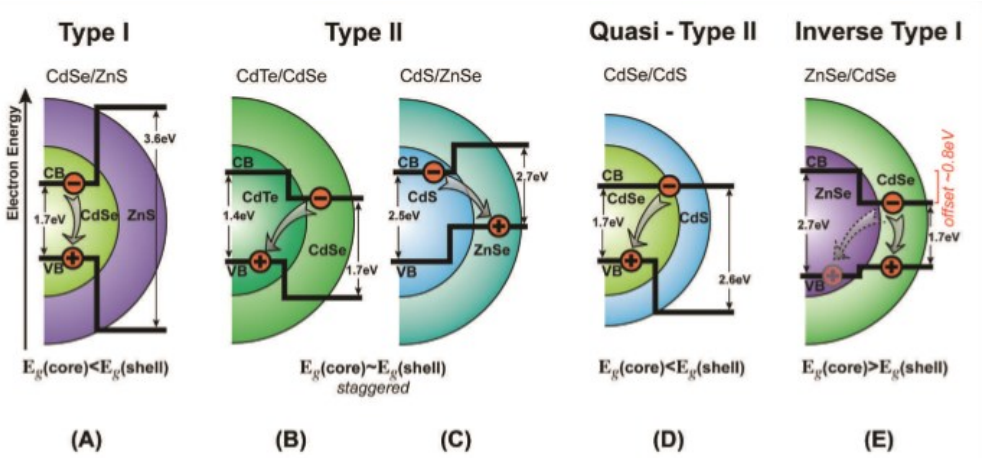

Figure 8: Types of quantum dots (A) Type I with localization of both carriers in the core (B) Type II with localization of the electron in the shell (C) Type II with localization of the hole in the shell (D) Quasi – Type II with localization of the electron in both the core and the shell (E) Inverse-Type I with localization of both carriers in the shell. Adapted from the [13].

Another way of affecting PL of SQDs is plasmon-coupled fluorescence. In that case, SQDs are immobilized on metallic nanostructures of thin films [9,10]. Kulakovich et al. observed enhancement of PL by factor 5, when the layer-by-layer assembly controllably places ZnCdSeS SQDs at fixed distance from Au NPs used [49]. Maximal signal of PL

of SQDs was observed at the 11 nm distance from Au NPs. More successful were Song et al. who observed 50-fold enhancement [50]. They used fabricated a periodic silver nanoisland array and when plasmonic features of substrate were in resonance with emission SQDs 655, they observed maximal enhancement of PL. A similar study was performed by Pompa et al. [51]. They observed 30-fold enhancement, when they coupled PL emission of SQDs 550,598,625 to plasmon resonance of a periodic nano-pattern of Au triangles. Also Leong et al observed 15-fold enhancement when SQDs were sandwiched between lithographic 2D array of Au nanodiscs and colloidal Au NPs with controlled spacing [52]. As the binding agent and the spacer between nanodiscs and colloidal Au NPs, peptides, such as biotin were used.

2.6. Assembling of NPs

Assembling of metal NPs or co-assembling of metal NPs with other types of NPs is an important issue in nanoscience. Assembled NPs could be prepared by several ways. However a large number of preparations is based on a similar principle, when hydrophilic surface of metal NPs is covered by hydrophobic molecules.

Whetten et al. prepared highly oriented Ag NPs by an aerosol processing approach [53]. At first elementary Ag was evaporated at high temperature in ultra-high purity helium, to prevent oxidation. The actual preparation provides relatively oriented and assembled NPs. Whetten at al. found, that condensation of Ag NPs in presence of alkylthiols, in particularly dodecanethiols, increases orderliness of Ag NPs.

Li et al. prepared several assembled metal NPs or SQDs by hydrothermal method, modified and called as liquid-solid-solution (LSS) method [54]. LSS method is called due to interfaces, which are crated in an autoclave – ethanol-linoleic acid liquid phase (liquid), metal linoleate (solid), and water-ethanol solutions (solution). Assembled nanoparticles modified by alkyl chains were created at the solid surface.

Assembling of Ag and Au NPs into 2D interfacial films at the interface between the plasmonic NPs hydrosol and a solution of an amphiphilic adsorbate in dichloromethane has also been reported [55 – 57].

Curri et al. also prepared highly oriented and assembled Au NPs by a simple drop-deposition on the substrate [58]. In general, Au NPs coated by oleyamine were dropped at the Si/SiO2 substrate and led to dry at hot plate. In their work, they have also studied the effect of the substrate surface chemistry and influence of NPs concentration, the

solvent and the temperature of evaporation of solvent. These types of preparation are potentially suitable for co-assembling of metal NPs with another types of NPs.

There is also an approach, where metal NPs are directly assembled with some fluorescence probe (most often with SQDs) by means of biologically important molecules such as glucose, amino acids or DNA, which function as link [59,60]. In those cases, the linker functions as a spacer and the main aims are targeted on metal enhanced fluorescence or study of fluorescence resonance energy transfer in biological systems.

3. Objectives

I. A Design and preparation of a new type of active surface based on purposefully modified and assembled Ag NPs in which „hot spots“ = nanoscale - localized strong optical fields will be generated by an external optical excitation

I. B Testing of the new active surface by SERS (Surface-enhancement Raman scattering), SERRS (Surface-enhanced resonance Raman scattering) and surface modified luminescence of a selected chromophoric and luminophoric adsorbate

II. A Co-assembling of Au NPs and semiconductor quantum dots (SQDs) into 2D arrays of various Au NPs : SQDs ratios

II. B Preliminary luminescence intensity measurements from selected co-assemblies of Au NPs and SQDs

4. Experimental

4.1. Materials

4.1.1. Chemicals

- Silver nitrate – $AgNO_3$ (Merck, p.a.)
- Hydroxylamine hydrochloride – $NH_2OH \cdot HCl$ (Sigma Aldrich)
- Sodium hydroxide – NaOH (Merck, p.a.)
- Tris(bipyridyl) Ru(II) dichloride – $[Ru(bpy_3)]Cl_2$ (Fluka)
- Hydrophobic Au nanoparticles, average size 6 – 7 nm (PlasmaChem)
- Hydrophobic ZnCdSeS alloyed quantum dots with 470, 532 and 610 nm emission maxima, diameter ca 6 nm (PlasmaChem)
- Nitric acid – HNO_3 (Lach-Ner, p.a.)
- Hydrochloric acid – HCl (Lach-Ner, p.a.)
- Sulphuric acid – H_2SO_4 (Lach-Ner, p.a.)
- Hydrogen peroxide – H_2O_2 (Lach-Ner, p.a.)
- Chromsulfuric acidic mixture (Lach-Ner, a.)
- Doubly distilled water
- Toluene for spectroscopy – C_7H_8 (Merck)
- Dichloromethane for spectroscopy – CH_2Cl_2 (Merck)
- Hexane – C_6H_{14} (Lach-Ner, p.a.)

4.1.2. Chemical glassware and cuvettes

All glassware was cleaned by a double distilled water, dilute nitric acid (1:1), peroxymonosulfuric acid, aqua regia and once again by the doubly distilled water. In each bath, the glassware was soaked at least for 30 minutes. Cuvettes for UV/vis measurements were also washed by chromsulfuric acid. Between immersions into each bath, the glassware was rinsed by deionised water and the final rinse was done by the doubly distilled water.

4.2. Preparations of Ag NPs nanosponge aggregates

4.2.1. Preparation of the parent Ag NPs hydrosol by reduction of $AgNO_3$ by $NH_2OH{\cdot}HCl$ (HA-Ag NPs hydrosol)

Ag NPs hydrosols were prepared by reduction of $AgNO_3$ by $NH_2OH{\cdot}HCl$. This procedure was described in ref. [61] and modified in ref. [62]. Briefly, 90.0 mL of 1.6×10^{-3} M $NH_2OH{\cdot}HCl$ was mixed with 0.3 mL of aqueous solution of 1M NaOH. Subsequently, 10.0 mL of 1×10^{-2} M $AgNO_3$ were added. Specifically, 10.4 mg of $NH_2OH{\cdot}HCl$ was dissolved in 90.0 mL of doubly distilled water. To this solution, 30 μL of 1M aqueous solution of NaOH prepared by dissolving of 0.2 g NaOH in 5.0 mL of double distilled water were added. After addition of NaOH, the solution pH changes into slightly alkaline, which is necessary for reduction of $AgNO_3$ by $NH_2OH{\cdot}HCl$. Subsequently, 10.0 mL of aqueous solution of $AgNO_3$ (prepared by dissolving of 33.9 mg of $AgNO_3$ in 20.0 mL of doubly distilled water) were added dropwise. Stirring of the reaction mixture was continued for 45 minutes. A glass stirring bar and 350 rpm rotation speed of the magnetic stirrer was used for stirring.

HA-Ag NPs hydrosol is yellow – brown coloured and opalescent as shown in Fig. 9 – A. TEM image of the deposited NPs is shown in Fig. 9 – B. The average size of Ag-NPs determined by the histogram in Fig. 9 – C is 27 nm.

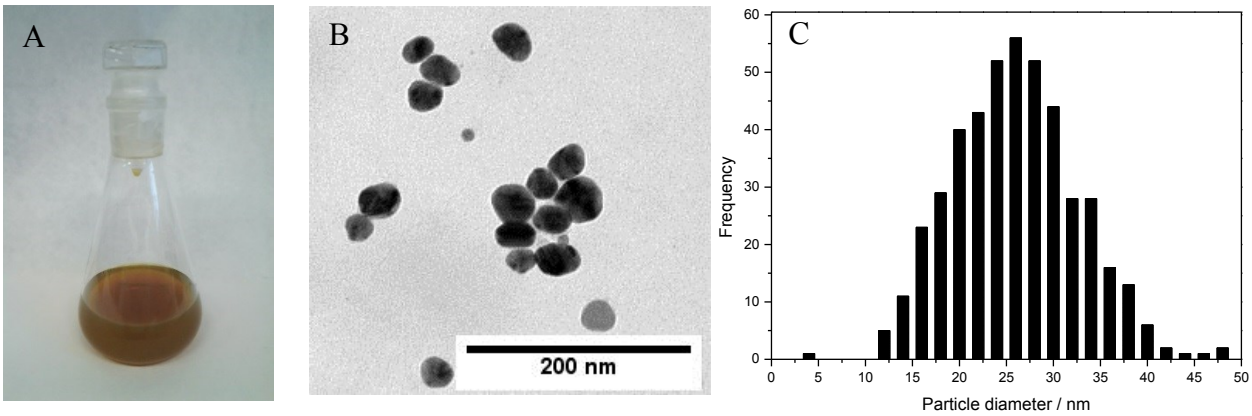

Figure 9: (A) HA-Ag NPs hydrosol (B) TEM images of Ag NPs from HA-Ag NPs hydrosol (C) Particle size distribution of HA-Ag NPs hydrosol

4.2.2. Preparation of 3D nanosponge aggregates with incorporated $[Ru(bpy)_3]^{2+}$ overlayed by a thin layer of aqueous phase as samples for measurements of the concentration dependence of SERS and SERRS spectra of $[Ru(bpy)_3]^{2+}$

Into a 5 mL weighting bottle, 2 mL of HA-Ag NPs hydrosol, 10.0 μL of 1M HCl aqueous solution and 20 μL of the $[Ru(bpy)_3]^{2+}$ aqueous solution of various concentrations were added. The final concentration of $[Ru(bpy)_3]^{2+}$ in the active system was varied in the 1×10^{-6} – 1×10^{-15} M range. The final concentration of HCl in all systems was 5×10^{-3} M. The closed weighting bottle was intensively manually shaken for 30 – 60 s, i.e. until formation of small fused aggregates was detected by the naked eye. A single 3D nanosponge Ag aggregate was prepared by merging of the fused aggregates by a pipette tip (1 – 1000 μL). Finally, the $[Ru(bpy)_3]^{2+}$ containing 3D nanosponge aggregate was transferred by a pipette tip onto a glass microscopic slide with a small amount (ca 50 μL) of the residual aqueous solution and employed as a sample for SERS and SERRS spectral measurement (Fig. 10) of $[Ru(bpy)_3]^{2+}$.

3D nanosponge aggregates with incorporated $[Ru(bpy)_3]^{2+}$ were prepared from the smallest concentration of $[Ru(bpy)_3]^{2+}$ in the active system to the highest value of concentration of $[Ru(bpy)_3]^{2+}$ (i.e. from 1×10^{-16} M to 1×10^{-6} M). Each measurement was repeated 10 times, to verify the purity and accuracy of the measurement.

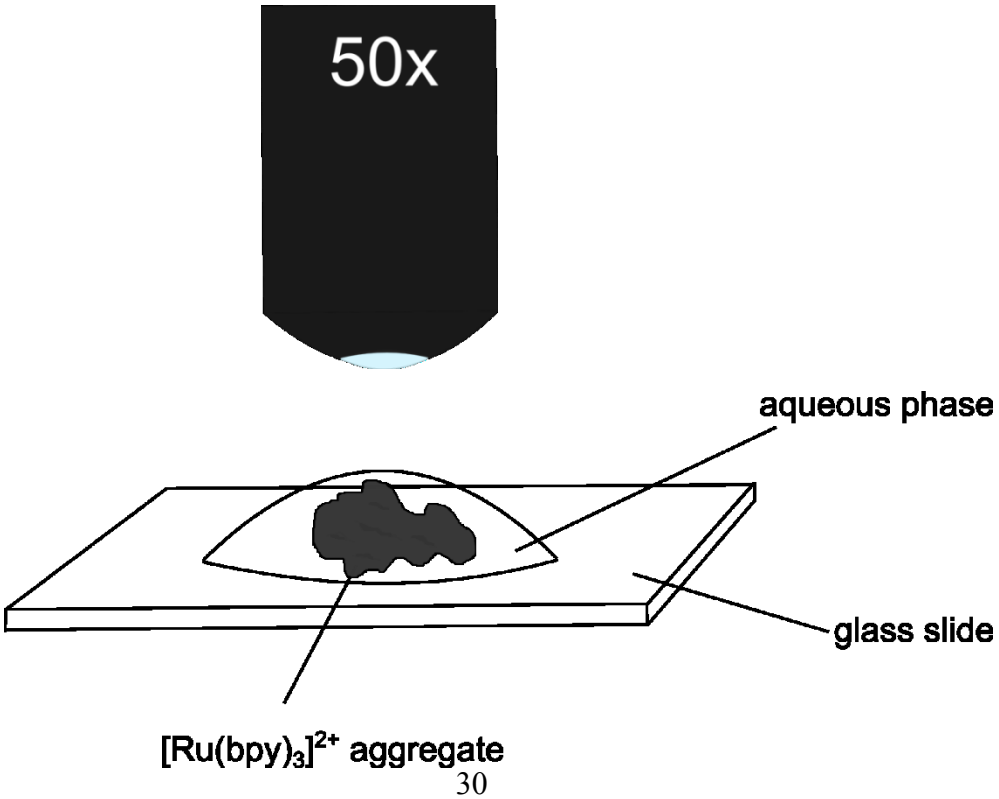

Figure 10: Graphical depiction of a 3D Ag nanosponge aggregate overlayed by a thin layer of aqueous phase on a glass slide.

4.2.3. Preparation of samples of 2D fused Ag NP aggregates for transmission electron microscopy (TEM)

For TEM imaging, the Electron Microscopy Sciences (CF400-Cu) copper grids were used. Into a 5 mL weighing bottle, 2 mL of HA-Ag NPs hydrosol,10.0 μL of 1M HCl aqueous solution and 20 μL of $[Ru(bpy)_3]^{2+}$ aqueous solution were added. After ca 1 min. of manual shaking, 10 μL of active system, containing 2D fused Ag NPs aggregates, was transferred to a copper grid. After 3 minutes of a gravitational deposition of the aggregates, the excess solution was removed by a filter paper from a copper grid.

4.2.4. Preparation of samples of 3D Ag nanosponge aggregates for scanning electron microscopy (SEM)

The $[Ru(bpy)_3]^{2+}$ containing 3D Ag nanosponge aggregates were prepared as described in the sub-chapter 4.2.2. After the transfer of the aggregate onto a glass slide, the residual aqueous solution was removed by a filter paper and the residues of the aqueous solution were left to dry.

4.2.5. Preparation of 3D nanosponge aggregates overlayed by a thin layer of aqueous solution of $[Ru(bpy)_3]^{2+}$ for surface – modified luminescence measurements

Into a 5 mL weighting bottle, 2 mL of HA-Ag NPs hydrosol and 10.0 μL of 1M HCl were added. The closed weighting bottle was intensively manually shaken for 30 – 60 s, till formation of small fused aggregates was observed. After formation of fused aggregates, 3D Ag nanosponge aggregates were created by merging of fused aggregates by a pipette tip (1 – 1000 μL). Subsequently, 3D nanosponge aggregate was transferred

by a pipette tip onto a glass slide covered with a thin layer of carbon. The residual aqueous solution was dried by filter paper and residues of the aqueous phase were left to dry. The dry 3D nanosponge aggregate was then overlayed by 20 μL of 1×10^{-5} M aqueous solution of $[Ru(bpy)_3]^{2+}$ and employed as a sample for luminescence measurements (Fig. 11).

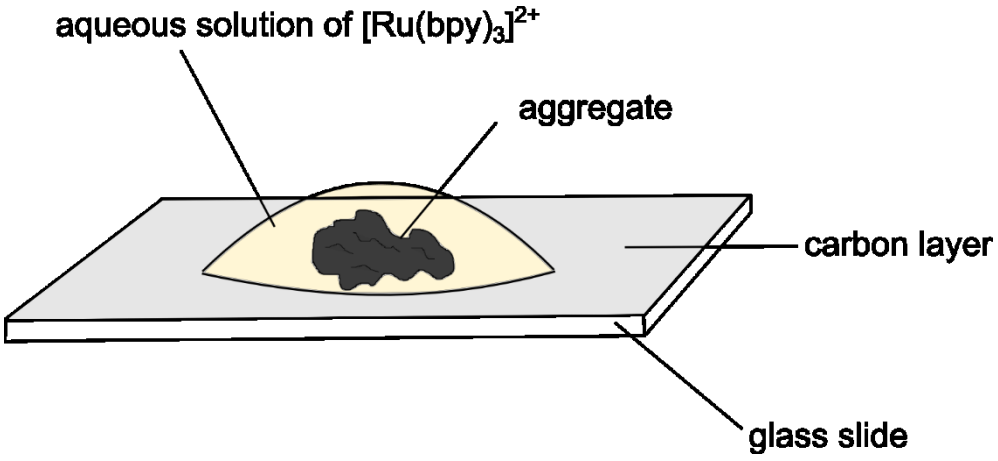

Figure 11: Graphical depiction of a 3D Ag nanosponge aggregate overlayed by a thin layer of 1×10^{-5} M $[Ru(bpy)_3]^{2+}$ aqueous solution on a glass slide covered by a carbon layer.

4.3. Assembling and co-assembling of hydrophobic Au NPs and semiconductor quantum dots

4.3.1 Assembling of hydrophobic Au nanoparticles

The first part of study of was focused on preparation of a monolayer of assembled hydrophobic Au NPs. Three types of organic solvent: hexane, toluene and dichloromethane were tested for dissolving of the hydrophobic Au NPs. Furthermore, solutions of Au NPs with different concentration of the NPs in the solution (organosols) were prepared. Summary of the prepared solutions is given in Tab. 1.

Table 1: Prepared solutions of hydrophobic Ag and Au NPs in different solvents

NPs	solvent	w%
Au	toluene	0.01
Au	toluene	0.05
Au	CH_2Cl_2	0.01
Au	CH_2Cl_2	0.05
Au	hexane	0.01
Au	hexane	0.05

4.3.2. Assembling of hydrophobic alloyed ZnCdSeS SQDs

Toluene was used as the solvent for dissolution of SQDs. Its choice is based on the results of the previous study of Au NPs and on the recommendation of the producer. Three types of SQDs differing by their emission maxima (470, 532 and 610 nm) were used. Concentrations (in w%) of the SQDs solutions (organosols) were the same as those of the Au NPs solutions as is demonstrated in Tab. 2.

Table 2: Prepared solutions of hydrophobic QDS in toluene

SQDs	solvent	w%
SQDs 470	toluene	0.01
SQDs 470	toluene	0.05
SQDs 532	toluene	0.01
SQDs 532	toluene	0.05
SQDs 610	toluene	0.01
SQDs 610	toluene	0.05

4.3.3. Co-assembling of Au NPs and SQDs

4.3.3.1. The interfacial films

Into a 7 mL vial, 300 μL of toluene solution of Au NPs (0.05 w%), 2.2 mL of CH_2Cl_2, 2.5 mL of doubly distilled water and 200 μL of toluene solution of SQDs (0.05 w%) were added. Then, the vial was intensively manually shaken until formation of a thin interfacial film. The film was transferred onto a glass slide by a pipette tip together with the residual water. From the film assembled on the surface of a water drop on the glass slide, TEM samples were prepared by briefly touching the film by a carbon coated Cu grid.

4.3.3.2. Co-assembling of Au NPs and SQDs on water surface

Samples for fluorescence measurement were prepared as follows: First, 5 mL of doubly distilled water were put into a vial. To the surface of the water phase, drops of toluene solutions of hydrophobic Au NPs (0.05 w%) and of SQDs (0.05 w%) were added by a pipette tip in the ratio shown in Tab. 3. Unfortunately, the molar ratios of Au NPs: alloyed ZnCdSeS SQDs could not be determined, since the actual composition of the ZnCdSeS alloy (i.e. the ZnCdSeS ratio) has not been provides by the producer.

Schematic depiction of co-assembling of Au NPs and SQDs at water surface is provided in Fig. 12. Samples for TEM imaging were obtained by submerging of the Cu-grid under the co-assembled particles which resulted into deposition of the assembly on the grid. Fluorescence intensity measurements were performed directly from the vial.

Table 3: Volumes of co-deposited Au NPs and SQDs solutions and Au NPs : SQDs weight ratios

Au:SQDs	Samples
1:1	2.5 µL Au NPs + 2.5 µL SQDs
1:2	2.0 µL Au NPs + 4.0 µL SQDs
1:4	1.0 µL Au NPs + 4.0 µL SQDs
1:6	0.5 µL Au NPs + 3.0 µL SQDs
1:8	0.5 µL Au NPs + 4.0 µL SQDs
1:10	0.5 µL Au NPs + 5.0 µL SQDs
2:1	4.0 µL Au NPs + 2.0 µL SQDs
4:1	4.0 µL Au NPs + 1.0 µL SQDs
6:1	3.0 µL Au NPs + 0.5 µL SQDs
8:1	4.0 µL Au NPs + 0.5 µL SQDs
10:1	5.0 µL Au NPs + 0.5 µL SQDs

Glass slides were used as supporting surfaces for preparation of samples for surface plasmon extinction (SPE) measurements. The co-assembling was accomplished by mixing of the toluene solutions of Au NPs and SQDs on a water drop deposited on the surfaces of the slides.

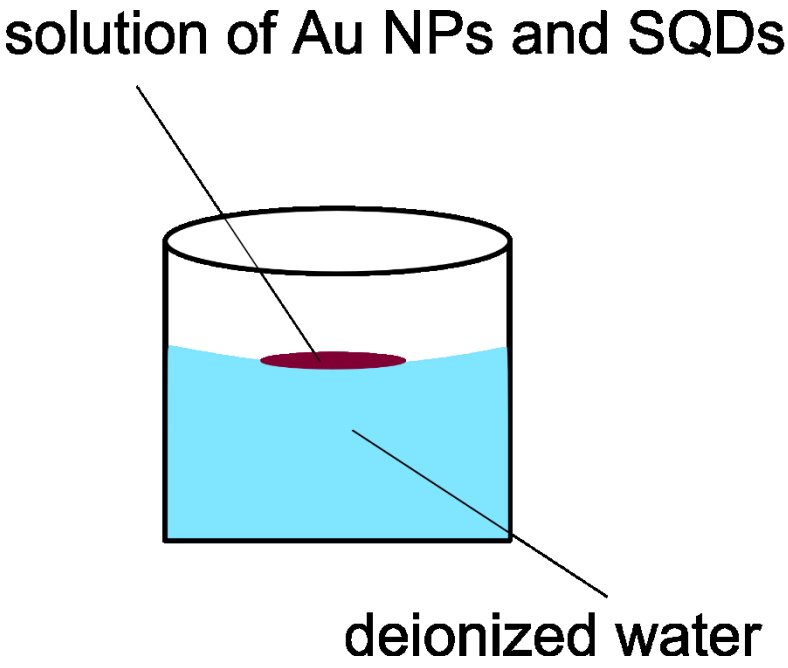

Figure 12: Schematic depiction of co-assembling of Au NPs and SQDs on the water surfaces

4.4. Instrumentation

4.4.1. Surface-enhanced Raman scattering and Surface-modified luminescence measurements

SERS and SERRS spectra were recorded on a DXR Raman microscope (Thermo Scientific) interfaced to an Olympus microscope. For SERS measurements, an objective with the 50x magnification was used. The 445 nm (diode laser), 532 nm (diode-pumped solid state laser), 633 (He-Ne laser) and 780 nm (diode laser) excitation lines were used.

The maximal laser power ranged from 8 to 24 mW. For luminescence measurements, an objective with the standard 10x magnification was employed. Excitation was provided by the 532 nm (diode-pumped solid state) laser with 0.5 mW power.

Full range gratings were used for all measurements.

4.4.2. UV/vis spectral measurements

UV/vis spectra measured from glass slides (solid samples) were recorded on a Specord s600 (Analytik Jena). UV/vis spectra measured in a quartz cuvette (liquid

samples) were recorded on a Schimadzu UV-2401 PC UV-VIS (Schimadzu corporation) recording spectrometer.

4.4.3. Transmission electron microscopy

TEM images were obtained with TECNAI G2 Spirit (FEI) transmission electron microscope with the acceleration voltage 120 keV.

4.4.4. Scanning electron microscopy

SEM images were obtained with Quanta 200 FEG (FEI) scanning electron microscope.

4.4.5. Optical microscopy

Optical images were obtained with Leica DM6000 M (Leica Microsystems) optical microscope.

4.4.6. Luminescence lifetime imaging microscopy and luminescence intensities measurements

Luminescence lifetime imaging (namely phosphorescence lifetime imaging – PLIM) measurements were performed using the laser scanning confocal microscope with inverted confocal microscope LSM FV1200 IX83 (Olympus) with PicoQuant (PicoQuant). The emitted light was separated from the excitation light by using a dichroic beam splitter (560 dcxr, PicoQuant) and the emitted light was filtered to detectors by FF01-520/35 and ET600/50M (PicoQuant) filters.

From PLIM measurements, two types of images were obtained. The first type of images are PLIM images with general lifetimes scale. The second type of images employs the amplitude scale, i.e. the one specific colour belongs to the one amplitude. From fitting of phosphorescence decay, lifetime to amplitude was assigned.

4.5. Processing of spectral and imaging data

For processing of the UV/vis spectra, first the Winaspect or the UVprobe programs were used and then OriginPro 9.0 was employed. For processing of SERS/SERRS spectra, first OMNIC program and then OriginPro 9.0 were used. The limits of SERS or SERRS spectral detection were determined as the lowest concentration of $[Ru(bpy)_3]^{2+}$ in the active system for which three characteristic marker spectral bands were observed.

Fluorescence intensities measurement were obtained and evaluated by FV10 program. FLIM and PLIM images were processed by the PicoQuant program. Emission and excitation spectra were evaluated in OriginPro 9.0.

Optical, SEM and TEM images and image analyses were processed in the NIS-Elements 4.0 program.

4.6. Calculation of enhancement factors in surface – modified luminescence

Enhancement factor (E_F) of surface modified luminescence (namely of the ^{3}MLCT phosphorescence) of $[Ru(bpy)_3]^{2+}$ in the vicinity of the Ag nanosponge aggregate was calculated using the carbon covered slide and the Ag nanosponge aggregate areas from which luminescence was collected, and intensities of luminescence measured from the selected areas on carbon and on Ag nanosponge aggregate by using the equation:

.

$$E_F = \frac{I_{agr}}{I_C} \cdot \frac{A_C}{A_{agr}}, \tag{4.1}$$

where I_{agr} and I_C are intensity of fluorescence measured from the Ag nanosponge aggregate and from the carbon layer, respectively. A_{agr} and A_C are the areas of Ag nanosponge aggregate and of the carbon layer, respectively, from which fluorescence intensity were measured.

The intensities and areas were calculated automatically by the FV10 program.

4.7. Calculation of fractal dimension

Fractal (Hausdorff) dimensions (D values) of the aggregates deposited from the *HA-Ag NP hydrosol/HCl/*$[Ru(bpy)_3]^{2+}$ system were determined from their TEM images using the mass–radius relation $M \sim R^D$ (where M is the mass of the object of size R) [63,64] and adopting a modification of the original procedure [65]. By the correspondence between the D value of the deposited aggregates determined from their TEM image and that determined for the aggregates in the hydrosol system reported for fractal aggregates of $D < 2$, Weitz et al. [64] have established TEM as a suitable method of determination of fractal dimensions of aggregates in hydrosol systems.

Fractal dimension was thus calculated by using the relation:

$$M = R^D \tag{4.2}$$

$$ln\, M = D \cdot ln\, R \tag{4.3}$$

Adopting the modification [65] of the original procedure [64], the *D* value of Ag aggregate was calculated as a slope of dependence

$$\ln(Area) = D \cdot \ln(\sqrt{MeasuredArea}\,, \tag{4.4}$$

where *MeasuredArea* means the area of a square measurement frame and *Area* means area, which is occupied by Ag NPs within the particular measurement frame.

4.8. Calculation of number of molecules incorporated in laser beam-illuminated volume of the 3D Ag nanosponge aggregate

Details of calculations of number of molecules incorporated into the 3D Ag nanosponge aggregate are provided in Supplement I. The goal of this calculations is to determine the approximate number of molecules, from which the SERRS signal of $[Ru(bpy)_3]^{2+}$ dications ("molecules") originates for Ag nanosponge aggregate assembled from the parent HA-Ag NPs hydrosol/HCl/$[Ru(bpy)_3]^{2+}$ systems with very low $[Ru(bpy)_3]^{2+}$ concentration, namely 1×10^{-14} M.

First, the illuminated volume of Ag nanosponge aggregate was considered to be ca 1 μm^3 (based on the technical parameters of the spectrometer). A simple approach, in which the volume (1.5 × 1 × 0.025 mm) of the overall 3D aggregate would be approximated by a block of a particular volume was considered to be too crude due to the irregular shape of the aggregate.

A more sophisticated approach thus had to be adopted. The approach is based on consideration that the fraction of Ag from the overall amount of Ag in the parent HA-Ag hydrosol system present in the laser-beam illuminated area of the aggregate is equal to the fraction of $[Ru(bpy)_3]^{2+}$ dications from the overall amount of $[Ru(bpy)_3]^{2+}$ in the parent system which is present in the illuminated aggregate area.

For determination of the former fraction (i.e. that of Ag), the TEM images of the fused 2D aggregates have been analysed and their 3D assembling was modelled by a cylindrical model of the layer – by layer assembling of 2D aggregates. The fraction of

Ag, and, consequently also of $[Ru(bpy)_3]^{2+}$ in the illuminated area is ca 2×10^{-8}, and the number or $[Ru(bpy)_3]^{2+}$ dications in 2 mL of 1×10^{-14} M solution is 1.2×10^{7} (i.e. in the parent HA-Ag NP hydrosol/HCl/$[Ru(bpy)_3]^{2+}$ system). This result indicates the presence of ca 0.3 molecules in the illuminated area. Therefore, statistically, only 1 of 3 or 4 measurements from different locations on the aggregate should yield the signal.

5. Results and discussion

5.1. 3D Ag nanosponge aggregates as samples for SERS and surface-modified luminescence (SML)

5.1.1. Morphological studies of 3D Ag nanosponge aggregate and its 2D fused Ag NPs aggregate precursors

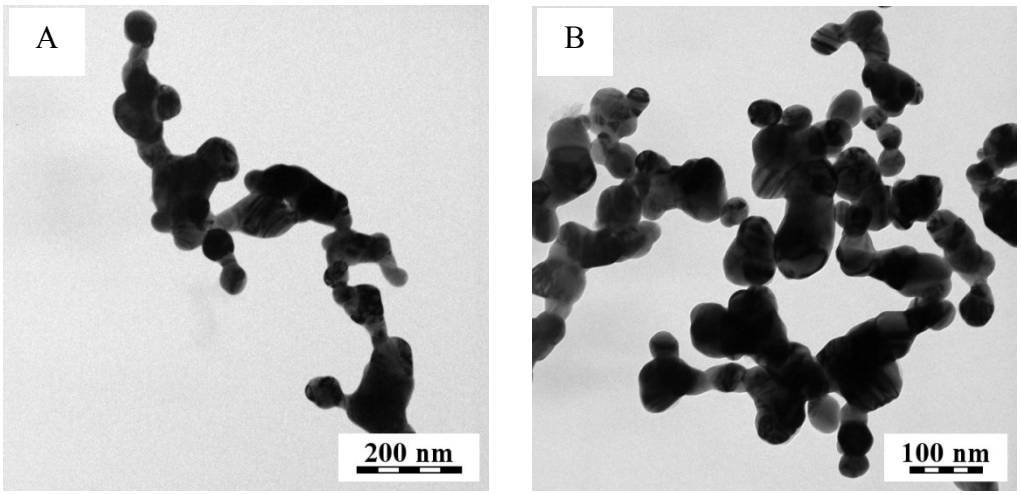

Figure 13: TEM images of fused Ag NPs aggregates prepared by modification of HA-Ag NPs hydrosol by addition of (A) HCl (B) HCl and $[Ru(bpy)_3]^{2+}$ aqueous solutions. The final concentration of HCl $c_M = 5\times10^{-3}$ M, of $[Ru(bpy)_3]^{2+}$ $c_M = 1\times10^{-8}$ M.

Modification of HA-Ag NPs hydrosol by HCl leads to an intergrowth of isolated NPs into 2D fused aggregates, as demonstrated in Fig. 13 – A . Further modification of HA-Ag NPs hydrosol by addition of $[Ru(bpy)_3]^{2+}$ aqueous solution does not change the morphology of Ag NPs aggregates, however it leads to a further intergrowth of Ag NPs aggregates as demonstrated in Fig. 13 – B.

It was important to establish whether the 2D fused aggregates are fractal objects. For this purpose, their fractal dimension (D) was determined by the procedure described in the Experimental section. For the calculation of average value of the fractal dimension, the TEM images of the 2D fused aggregates deposited from the HA-Ag NPs hydrosol/HCl (5×10^{-3}) M/$[Ru(bpy)_3]^{2+}$ (1×10^{-8} M) (Fig. 14) were used.

The average value of the fractal dimension D = 1.87 ± 0.02. The fractal character of these aggregates indicates that after optical excitation, “hot spots” will be generated in them [15,16,28,41] .

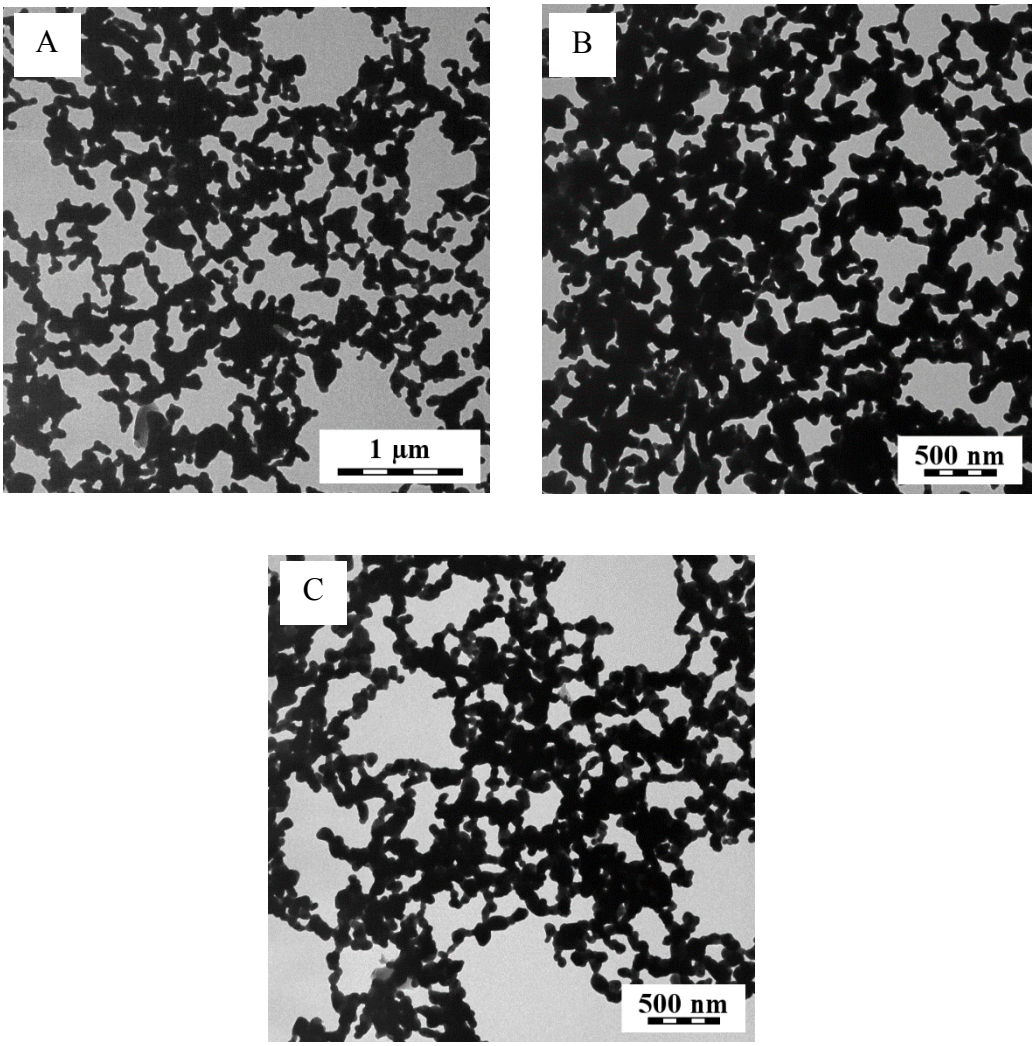

Figure 14: A – C: TEM images of 2D fused Ag NPs aggregates prepared from HA-Ag NPs hydrosol/HCl (5×10^{-3} M)/ $[Ru(bpy)_3]^{2+}$ (1×10^{-8} M) system

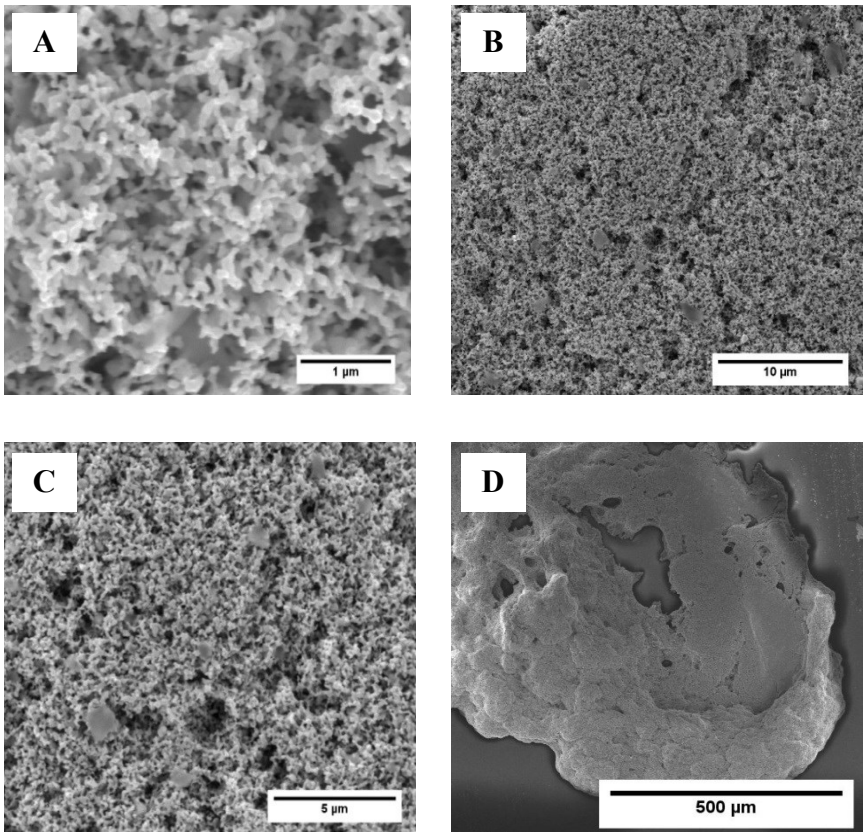

Figure 15: SEM images of 3D Ag nanosponge aggregate prepared from the 2D fused aggregates formed in the HA-Ag NPs hydrosol/HCl (5×10^{-3} M)/ $[Ru(bpy)_3]^{2+}$ (1×10^{-8} M) system (A) 30 000x (B) 8000x (C) 4000x (D) 100x magnification

SEM images (Fig. 15) show a 3D nanosponge Ag aggregate prepared by assembling of fused Ag NPs aggregates. The images A – C in Fig. 15 demonstrate the nanosponge internal morphology of the 3D Ag aggregate. A comparison of the SEM images of the 3D Ag nanosponge aggregate (Fig. 15) with the TEM images of fused Ag NPs aggregates deposited from HA-Ag NPs hydrosol/HCl/$[Ru(bpy)_3]^{2+}$ systems (Figs 13 and 14) indicates that the nanosponge morphologies of the macroscopic aggregates (1 – 3 mm in size, Fig. 15 – D) were formed by the 3D bottom-up assembling of the fractal building blocks.

For characterization of the internal morphology of the nanosponge aggregates, the pore sizes were determined. Two types/sizes of pores were found and their average values were determined: smaller pores with average size about 50 nm and larger pores with average size about 200 nm, as demonstrated by the histogram in Fig. 16.

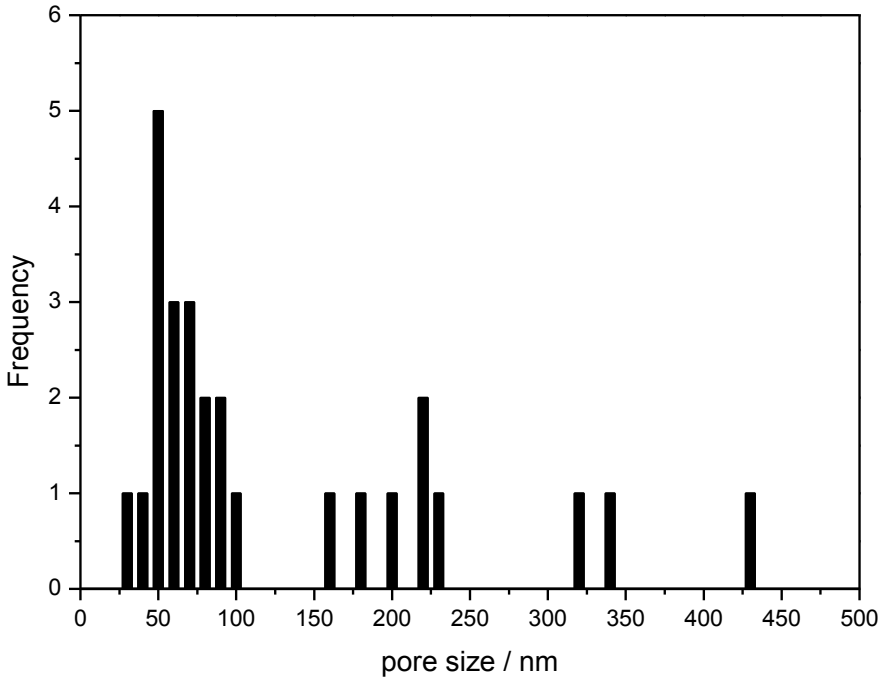

Figure 16: Histogram of pore size distribution in Ag nanosponge aggregate

5.1.2. SPE spectra

First, SPE (surface plasmon extinction) spectra of the parent HA-Ag NPs hydrosol, HA-Ag NPs hydrosol/HCl and of HA Ag-NPs hydrosol/HCl/$[Ru(bpy)_3]^{2+}$ active systems with concentrations of $[Ru(bpy)_3]^{2+}$ aqueous solutions in the 1×10^{-6} – 1×10^{-16} M range were measured and they are presented in Fig. 17. HA-Ag NPs hydrosol shows one extinction maximum at 402 nm. SPE spectra show, that addition of HCl and $[Ru(bpy)_3]^{2+}$ causes a decrease of the original extinction maximum and an increase of extinction in the 500 – 800 nm range. These changes in the active systems extinction indicate a formation of aggregates. Addition of HCl affects the Ag NPs hydrosol the most. It means that it causes a drastic change of extinction, while addition of the testing adsorbate causes further changes, however, not so dramatic.

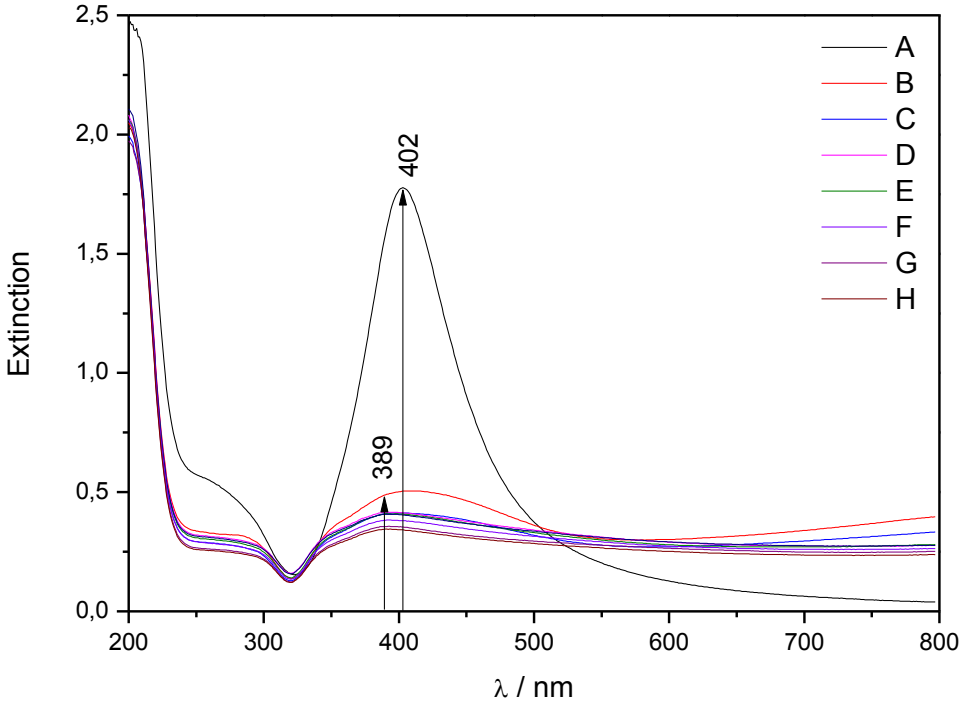

Figure 17: SPE spectra of (A) HA-Ag NPs hydrosol (B) HA-Ag NPs hydrosol/HCl and (C – H) HA Ag-NPs hydrosol/HCl/$[Ru(bpy)_3]^{2+}$ active systems. Final concentration of $[Ru(bpy)_3]^{2+}$ in the active systems was (C) 1×10^{-6} M (D) 1×10^{-8}M (E) 1×10^{-10} M (F) 1×10^{-12} M (G) 1×10^{-14} M (H) 1×10^{-16} M

SPE spectrum of Ag nanosponge aggregate (Fig. 18) shows an increase of extinction in the 400 – 500 nm range, while the value of extinction in the range 500 – 800 nm only slightly decreases with the increasing wavelength.

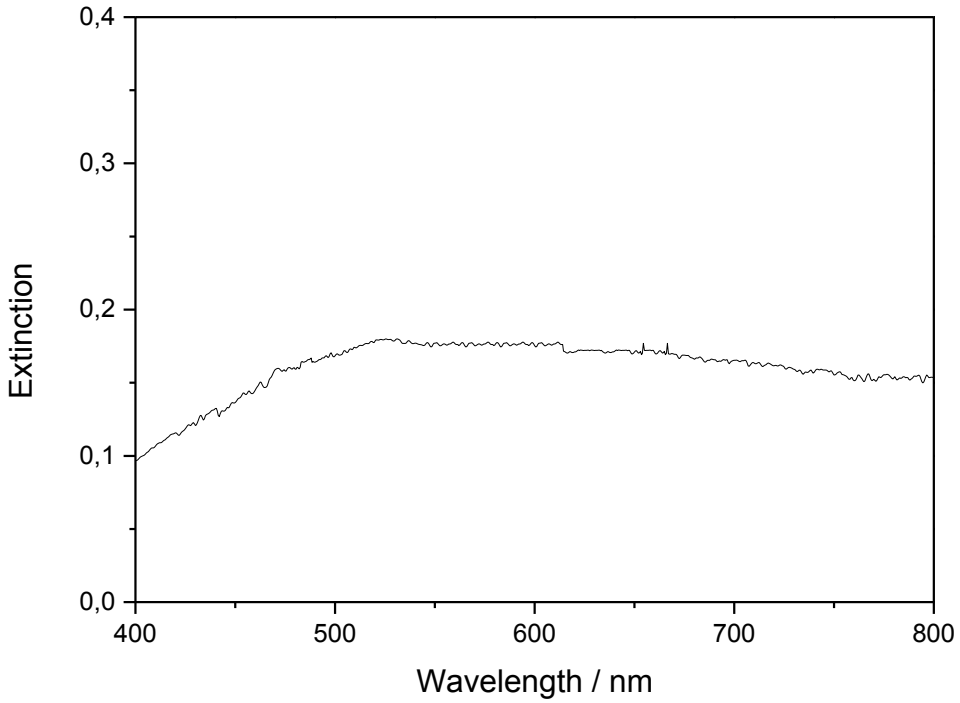

Figure 18: SPE spectra of 3D nanosponge Ag aggregate.

5.1.3. SERS spectra of $[Ru(bpy)_3]^{2+}$ measured as function of $[Ru(bpy)_3]^{2+}$ concentration from Ag nanosponge aggregate overlayed by a thin layer of aqueous phase and determination of SERS and SERRS spectral limits of detection

SERS and SERRS spectra of $[Ru(bpy)_3]^{2+}$ from 3D nanosponge aggregate overlayed by a thin layer of aqueous phase were measured at four excitation wavelengths – 445, 532, 633 and 780 nm. Electronic absorption spectra of 1×10^{-6} M aqueous solution of $[Ru(bpy)_3]^{2+}$ and projections of the excitation wavelengths used for SERS and SERRS measurements are shown in Fig 19. The 780 nm and 633 nm wavelengths are well outside the electronic absorption band (Fig. 19), hence SERS spectra are obtained at these excitation wavelengths. The 532 nm wavelength falls within the outset of the electronic absorption band of the complex (Fig. 19). In accord with refs [22,23], a weak molecular resonance contribution to the overall signal has been encountered at this wavelength, hence the spectra measured at 532 nm are denoted as SER(R)S spectra. Finally, the 445 nm excitation is very close to the maximum of the $[Ru(bpy)_3]^{2+}$ electronic absorption band, therefore, SERRS spectra with a substantial molecular resonance contribution to the overall enhancement are obtained at this wavelength (Fig. 19). For each excitation wavelength, the limit of the SERS, SER(R)S or SERRS spectral detection was determined.

Fig. 20 shows SER(R)S spectrum of $[Ru(bpy)_3]^{2+}$ obtained from a Ag nanosponge aggregate assembled from the HA-Ag NPs hydrosol/HCl/1×10^{-8} M $[Ru(bpy)_3]^{2+}$ system measured at λ_{exc} = 532 nm. The characteristic spectral bands in SE(R)RS spectra of $[Ru(bpy)_3]^{2+}$ obtained from the Ag nanosponge aggregate at 532 nm excitation are compared to the previously published SE(R)RS spectra of $[Ru(bpy)_3]^{2+}$ measured from the Ag hydrosol/HCl/$[Ru(bpy)_3]^{2+}$ system [23], as well as to the RRS spectra of $[Ru(bpy)_3]^{2+}$ in solution (used as the input for the NCA calculation [11]) in Tab.4. The comparison reveals a very good (within 3 cm^{-1}) agreement between the SE(R)RS spectra measured from the Ag aggregate and from the hydrosol system at the same wavelength (532 nm), as well as a reasonably good agreement with the RRS spectra measured at 457.9 nm. (Tab. 4) These results provide evidence that $[Ru(bpy)_3]^{2+}$ dications are incorporated into the Ag nanosponge aggregates without perturbation of their native structure.

The characteristic bands at 1603, 1556, 1486 and 1317 cm^{-1} were used for determination of SERS, SER(R)S and SERRS spectral limits of detection.

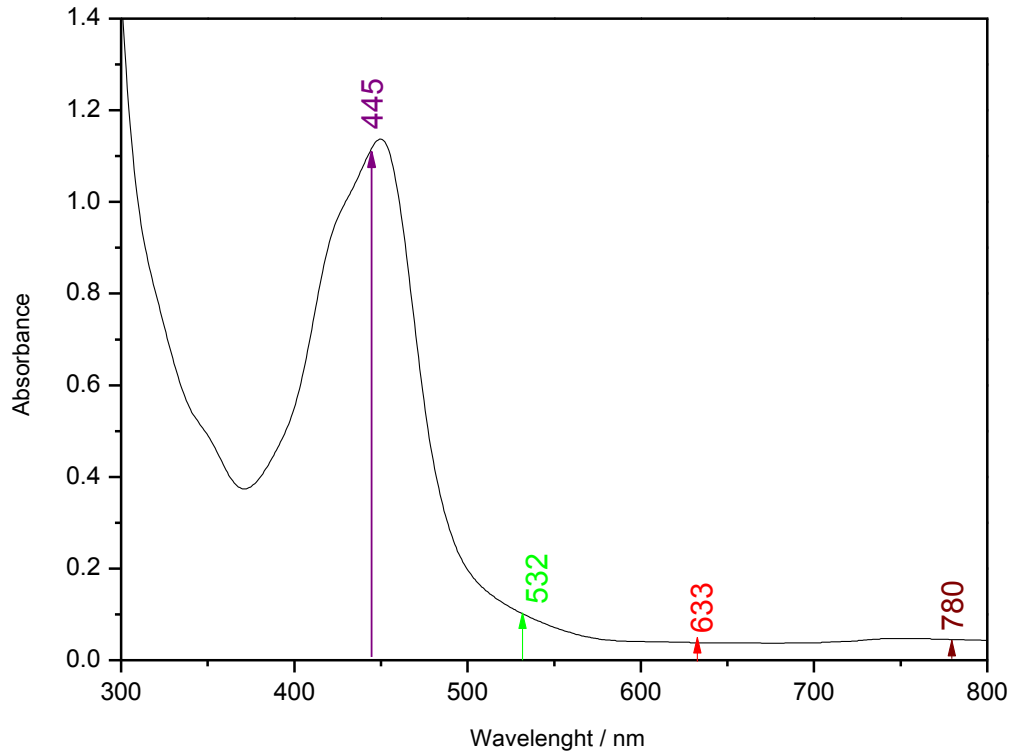

Figure 19: Electronic absorption spectra of 1×10^{-6} M aqueous solution of $[Ru(bpy)_3]^{2+}$ and projection of excitation wavelengths used for SERS, SER(R)S and SERRS measurements.

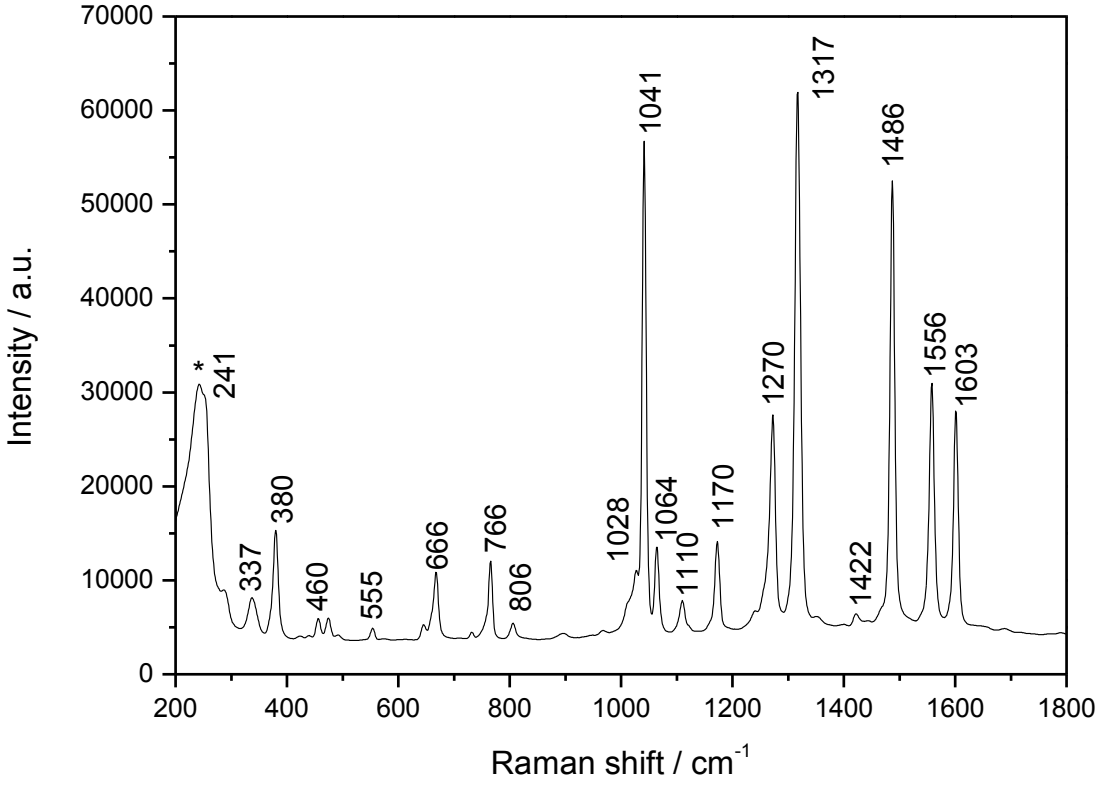

Figure 20: SERRS spectra of $[Ru(bpy)_3]^{2+}$ obtained from Ag nanosponge aggregate prepared from HA-Ag NPs hydrosol/HCl/1×10^{-8} M $[Ru(bpy)_3]^{2+}$ active system (λ_{exc} = 532 nm). The 240 cm^{-1} band of Ag-Cl vibration is marked by asterisk.

Table 4: Wavenumbers of $[Ru(bpy)_3]^{2+}$ bands observed in SER(R)S spectra in comparison to the previously published data

3D Ag nanosponge aggregate λ_{exc} = 532 nm SER(R)S	Ag hydrosol [23] λ_{exc} = 532 nm SER(R)S	Aqueous solution [11] NCA/RR
380	379	370 A_1
666	667	668 A_1
766	766	766 A_1
806	806	
1028	1025	1028 A_1
1041	1041	1043 A_1
1064	1064	1067 A_1
1110	1109	
1170	1172	1176 A_1
1270	1273	1276 A_1
1317	1317	1320 A_1
1486	1487	1491 A_1
1556	1558	1563 A_1
1603	1602	1608 A_1

SERS, SER(R)S and SERRS spectra of $[Ru(bpy)_3]^{2+}$ measured from a Ag nanosponge aggregate at concentrations corresponding to concentration values of SERS, SER(R)S and SERRS spectral limits of detection together with the Ag – Cl spectral band at 241 cm^{-1} are shown in Fig. 21. The same spectra without the Ag – Cl band, i.e. in the 300 – 1800 cm^{-1} are shown in Fig. 22. The following limits of SERS spectral detection of $[Ru(bpy)_3]^{2+}$ were determined: 8×10^{-11} M SERS at λ_{exc} = 780 nm (Figs. 21 and 22 (A)), 5×10^{-13} M SERS at λ_{exc} = 633 nm (Figs. 21 and 22 (B)), 1×10^{-14} M SER(R)S at λ_{exc} =532 nm (Figs. 21 and 22 (C)) and 1×10^{-15} M SERRS at λ_{exc} = 445 nm (Figs. 21 and 22 (D)).

Figure 21: SERS, SER(R)S and SERRS spectra of $[Ru(bpy)_3]^{2+}$ in limit of detection (LOD) at four excitation wavelengths. (A) λ_{exc} = 780 nm, LOD = 8×10^{-11} M (B) λ_{exc} = 633 nm, LOD = 5×10^{-13} M (C) λ_{exc} = 532 nm, LOD = 1×10^{-14} M (D) λ_{exc} = 445 nm, LOD = 1×10^{-15} M. The band at 241 cm^{-1}, which is marked by asterisk belongs to Ag – Cl vibration.

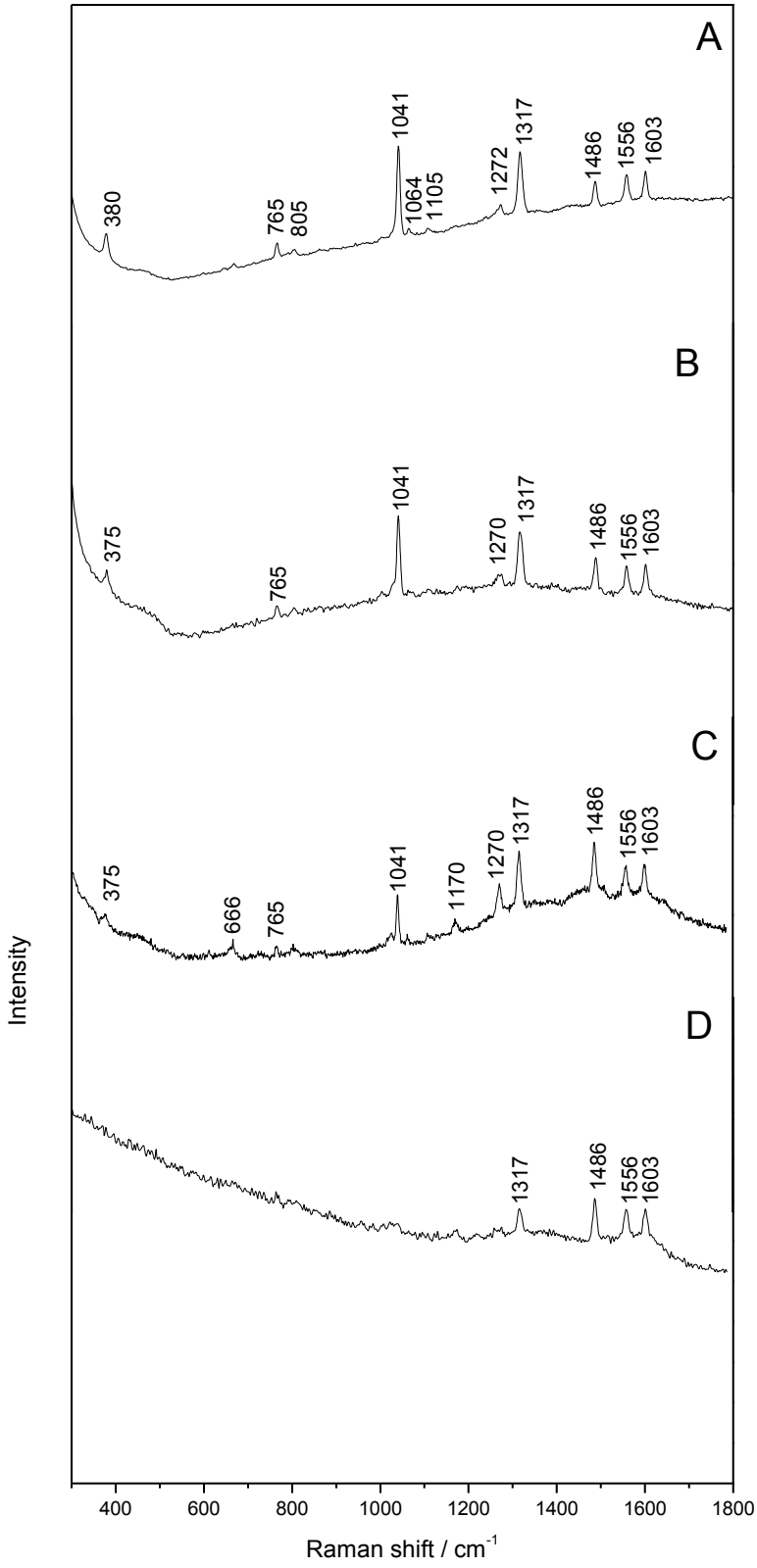

Figure 22: SERS, SER(R)S and SERRS spectra of $[Ru(bpy)_3]^{2+}$ in limit of detection (LOD) at four excitation wavelengths. (A) λ_{exc} = 780 nm, LOD = 8×10^{-11} M (B) λ_{exc} = 633 nm, LOD = 5×10^{-13} M (C) λ_{exc} = 532 nm, LOD = 1×10^{-14} M (D) λ_{exc} = 445 nm, LOD = 1×10^{-15} M.

The calculations outlined in the Experimental Section (Chapter 4.8) and presented in detail in Supplement I have shown, that from 3D Ag nanosponge aggregates in which the concentration of incorporated of $[Ru(bpy)_3]^{2+}$ 1×10^{-14} M, SERS or SERRS spectra on a single molecule level are obtained. In this work, such single molecule SER(R)S and SERRS spectra were obtained at 532 and 445 nm excitations. In particular, the 1 x 10^{-14} M limit of SE(R)RS spectral detection at 532 nm excitation corresponds to the presence of about 0.3 $[Ru(bpy)_3]^{2+}$ dications within the laser beam illuminated area of the Ag nanosponge aggregate (Chapter 4.8 and Supplement I).

As the evidence of single molecule SERS, sampling measurements and their statistical evaluation were done from Ag nanosponge aggregate overlayed by a thin layer of aqueous phase containing $[Ru(bpy)_3]^{2+}$ in the final concentration 1×10^{-14} M at λ_{exc} = 532 nm. Because of the 3D structure of the aggregate, it was not possible to do a SERS spectral mapping. For this reason, point by point measurements were done, i.e. the SERS signal was measured from several different points at the aggregate. This testing was done for three different aggregates and then the statistical evaluation of the signal was done. Fig. 23 demonstrates the results of the sampling for one of the tested aggregates. Fig 23 shows that from 12 measurements, the SERRS signal of $[Ru(bpy)_3]^{2+}$ was obtained only twice. There is thus about 17 % probability of finding $[Ru(bpy)_3]^{2+}$ signal within the aggregate, and the observed $[Ru(bpy)_3]^{2+}$ signal originates most probably from a single $[Ru(bpy)_3]^{2+}$ dication. Similar results were obtained for the other two aggregates. The achievement of the single molecule (molecular ion) level of detection is attributed to a combination of three effects: (i) localization of $[Ru(bpy)_3]^{2+}$ dications into “hot spots” in the fractal (D = 1.87 ± 0.02) fused 2D aggregates, from which the 3D nanosponge aggregate was assembled, (ii) very efficient accumulation of hots spots into the focus of the laser beam in SERS micro-Raman spectral measurements from the nanosponge aggregate, (iii) molecular resonance contribution to the overall SERS enhancement. In the last mentioned case, the one order of magnitude lower limit of SERRS spectral detection at 445 nm than that of the SE(R)RS spectral detection at 532 nm (which corresponds to ca one order of magnitude higher SERRS enhancement) is consistent with localization of the excitation almost into the maximum in the electronic absorption band in the former case, and only into the onset of the absorption band in the latter case (Fig. 19).

Furthermore, no spurious bands such as the broad bands of amorphous carbon were encountered in the SERRS, SE(R)RS and SERS spectra of $[Ru(bpy)_3]^{2+}$ (Figs. 20,21 and 22). These results indicate that the spectra were obtained without any $[Ru(bpy)_3]^{2+}$ decomposition during the measurements, and they are attributed to the presence of the thin aqueous phase layer preventing the thermal decomposition of the adsorbate.

In summation, SERS and SERRS spectral probing of $[Ru(bpy)_3]^{2+}$ containing Ag nanosponge aggregate has demonstrated the following advantages of SERS micro-Raman spectral measurements from the liquid overlayed, analyte (adsorbate) containing Ag nanosponge aggregate: (i) an efficient localization of the analyte, i.e. of the $[Ru(bpy)_3]^{2+}$ dication, into "hot spots" (ii) fast sample preparation, minimization of its volume and accumulation of "hot spots" into the focus of the laser beam (iii) single molecule level of the SERRS and SE(R)RS spectral detection of the analyte (iv) elimination of the analyte decomposition in "hot spots".

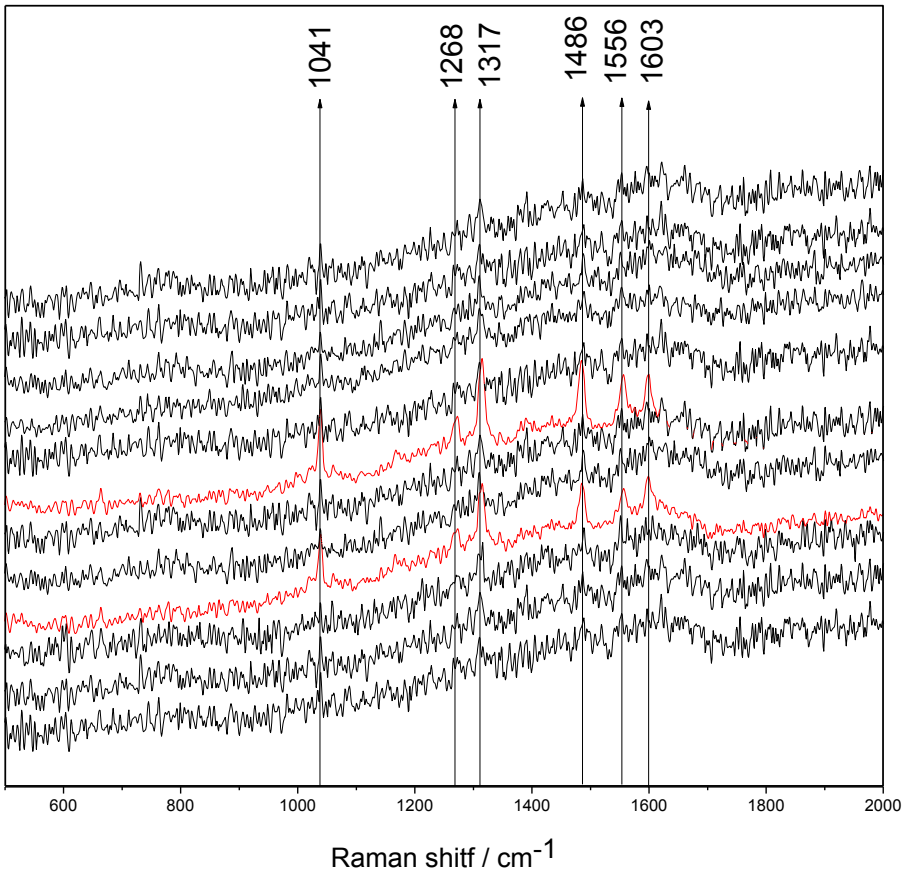

Figure 23: SER(R)S spectral sampling of an isolated 3D Ag nanosponge aggregate containing 1×10^{-14} M $[Ru(bpy)_3]^{2+}$ overlayed by a thin layer of aqueous phase measured at λ_{exc} = 532 nm.

5.1.4. Luminescence measurements from Ag nanosponge aggregates overlayed by a 1×10^{-5} M $[Ru(bpy)_3]^{2+}$ aqueous solutions

5.1.4.1. Phosphorescence intensity measurements

The first part of luminescence measurement was focused on the ^{3}MLCT phosphorescence intensities measurements of 1×10^{-5} M $[Ru(bpy)_3]^{2+}$ aqueous solution overlayed over the Ag nanosponge aggregate. From λ-scan measurements, the emission intensity images (Figs. 25 and 27) and the emission spectra (Fig. 24) of the typical sample (in which the aggregate was deposited on glass slide covered by a thin carbon layer) were obtained. The emission spectra in Fig. 24 demonstrate that the emission maximum of $[Ru(bpy)_3]^{2+}$ is at 620 nm.

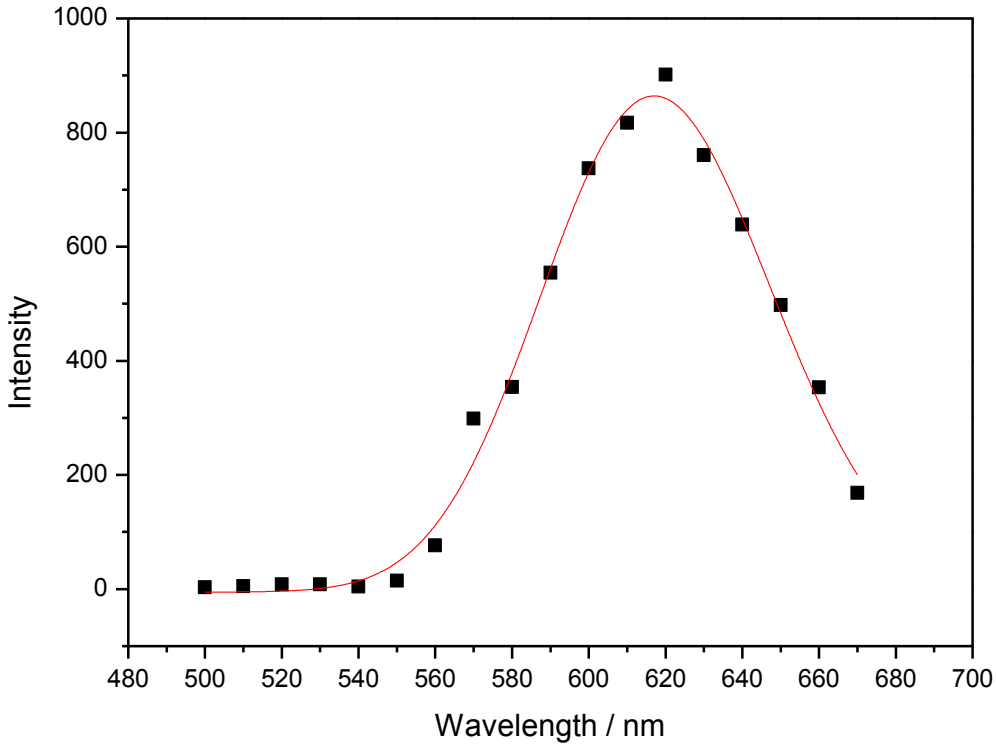

Figure 24: Emission spectrum of 1×10^{-5} M $[Ru(bpy)_3]^{2+}$ aqueous solution overlayed over the Ag nanosponge aggregate on the glass slide coated by the carbon layer.

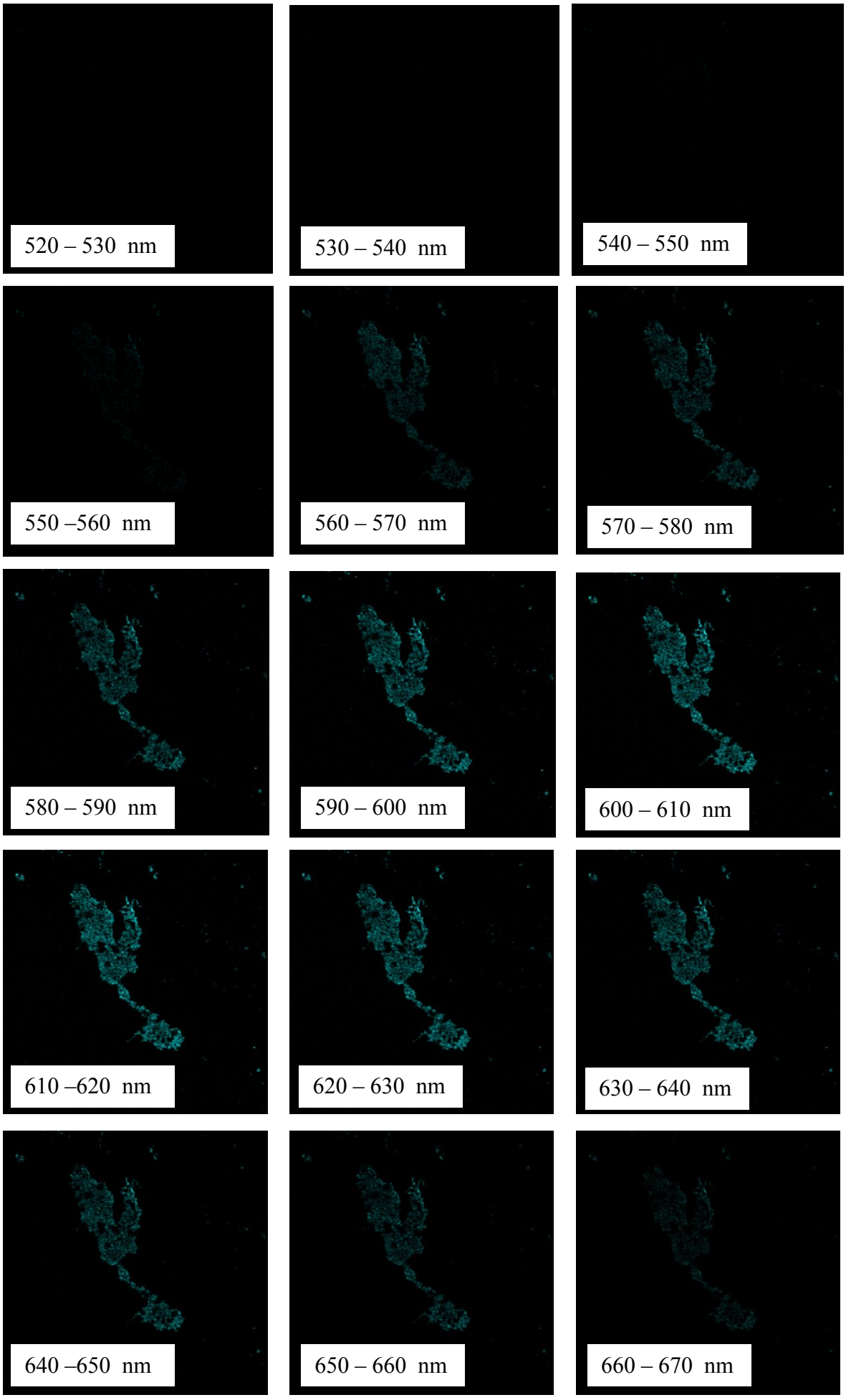

Figure 25: λ-scan images of Ag nanosponge aggregate at glass slide coated by carbon layer overlayded by a thin layer of 1×10^{-5} M $[Ru(bpy)_3]^{2+}$.

Figs. 26 and 27 demonstrate λ-scan measurements of Ag nanosponge aggregate overlayed by a thin layer of 1×10^{-5} M $[Ru(bpy)_3]^{2+}$ on a purposefully disturbed layer of carbon coating on the glass slide. The λ-scans were obtained from 3 surface locations of different sizes overlayed by the $[Ru(bpy)_3]^{2+}$ solution: the glass slide, the carbon layer and the aggregate (Figs. 26 and 28). The red plot of the phosphorescence intensity as a function of the emission wavelength (Fig. 28) demonstrates, that although the sampled area on the aggregate was the smallest of all, the signal is the highest (Figs. 26 and 28). The λ-scan measurements prove that surface-enhanced phosphorescence is observed from the $[Ru(bpy)_3]^{2+}$ cations located of the vicinity of the nanosponge Ag aggregate.

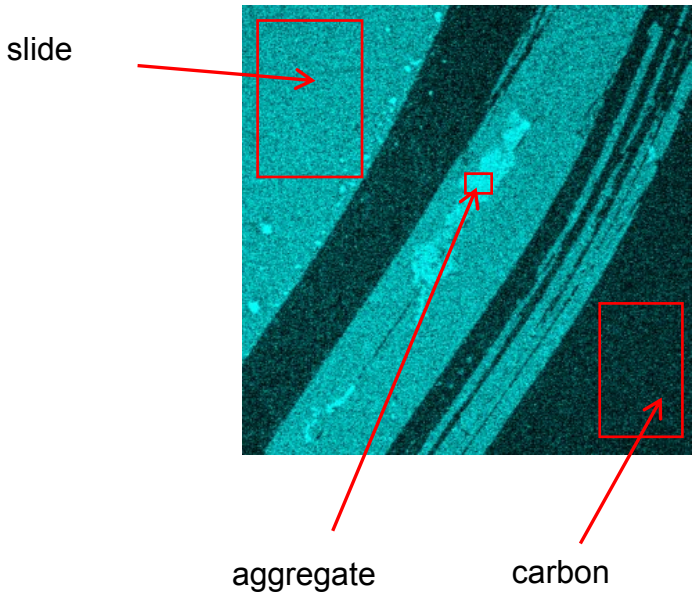

Figure 26: λ-scan image of Ag nanosponge aggregate on the glass slide coated by the carbon layer overlayded by a thin layer of 1×10^{-5} M $[Ru(bpy)_3]^{2+}$.

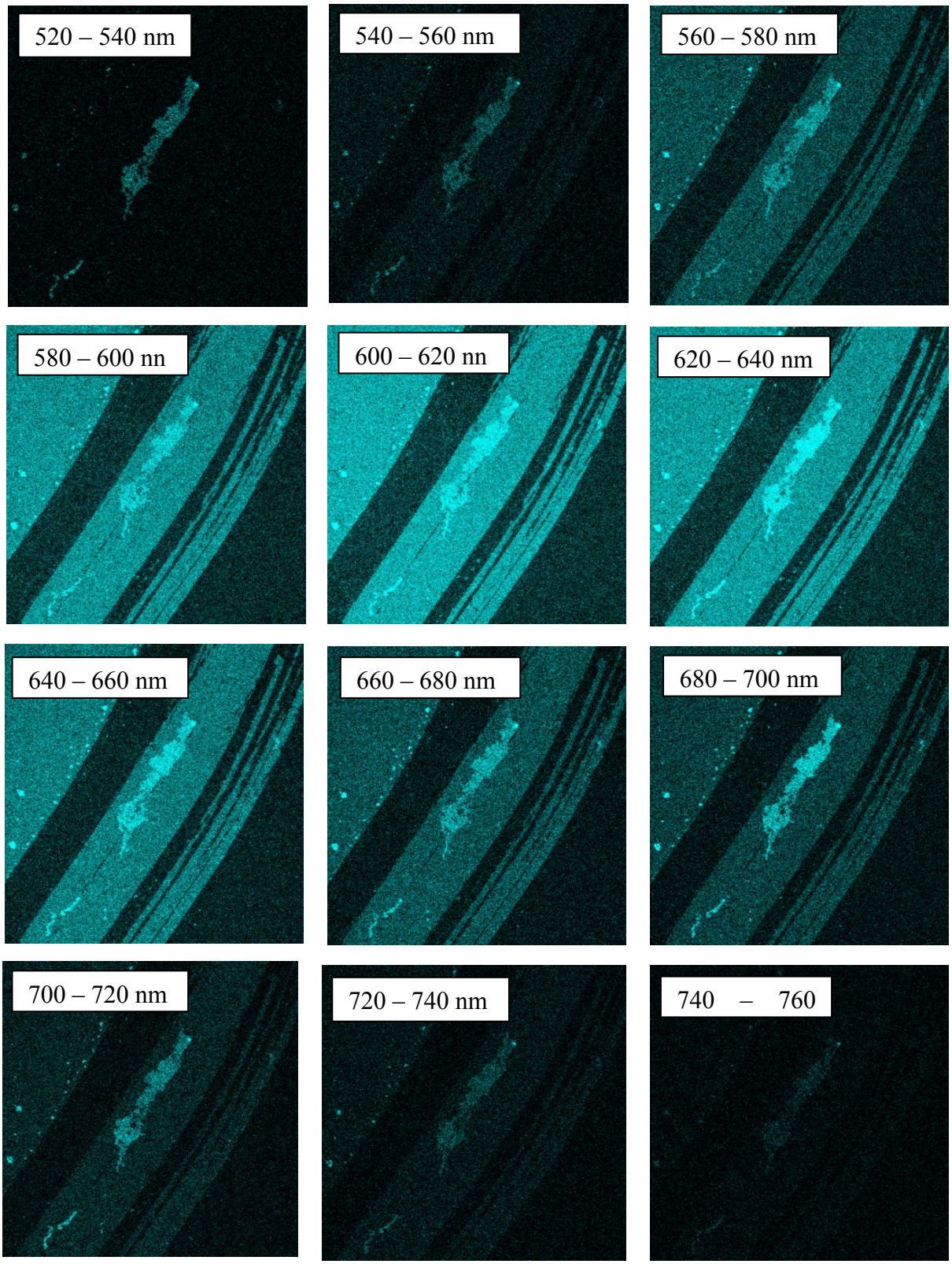

Figure 27: λ-scan images of Ag nanosponge aggregate on the glass slide coated by the carbon layer overlayded by a thin layer of 1×10^{-5} M $[Ru(bpy)_3]^{2+}$.

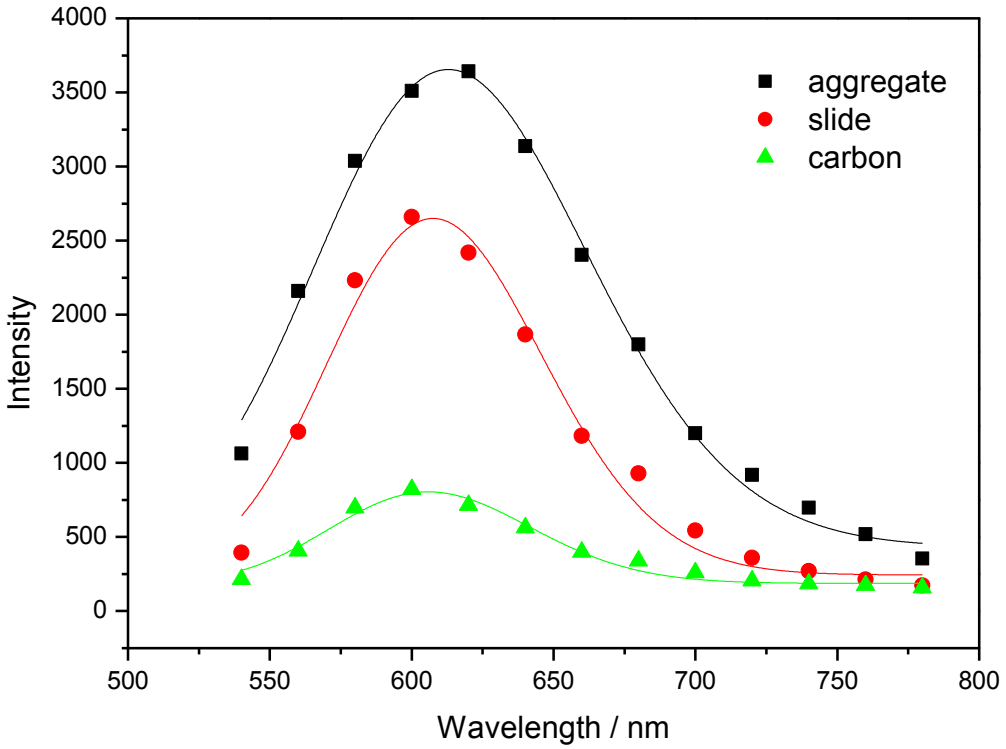

Figure 28: Emission spectra of 1×10^{-5} M $[Ru(bpy)_3]^{2+}$ aqueous solution overlayed over Ag nanosponge aggregate obtained from three different places. Locations: ■ aggregate, ● glass slide, ▲ carbon

Table 5: Intensity of phosphorescence in dependence on the supporting surface material and size of measured area

Material	Area / μm²	Intensity of phosphorescence
glass	1748	2353
carbon layer	1697	712
Ag aggregate	128	3756

Emission spectra of $[Ru(bpy)_3]^{2+}$ aqueous solution measured from the glass slide are affected by sedimentation of $[Ru(bpy)_3]^{2+}$ onto the glass slide. For this reason, each glass slide for the phosphorescence measurement was covered by a carbon layer. Tab. 5 relates the intensity of phosphorescence to the area of glass slide, of the carbon layer and of the Ag nanosponge aggregate. From the relationship between the intensity of phosphorescence and of the area of carbon layer and Ag aggregate, enhancement factor

of phosphorescence from the Ag nanosponge aggregate was calculated. The calculated value of enhancement factor is 70.

The SPE spectra of the Ag nanosponge aggregate with projections of the excitation wavelength (485 nm) and of the wavelength of the emission maximum at 620 nm (Fig. 29) demonstrate the overlaps of the SPE of the aggregate with both excitation (i.e. absorption) and phosphorescence of $[Ru(bpy)_3]^{2+}$. Both the $[Ru(bpy)_3]^{2+}$ absorption and phosphorescence can be enhanced by localization of the complex dications into the vicinity of the Ag nanosponge aggregate, and can thus contribute to the observed $[Ru(bpy)_3]^{2+}$ phosphorescence enhancement.

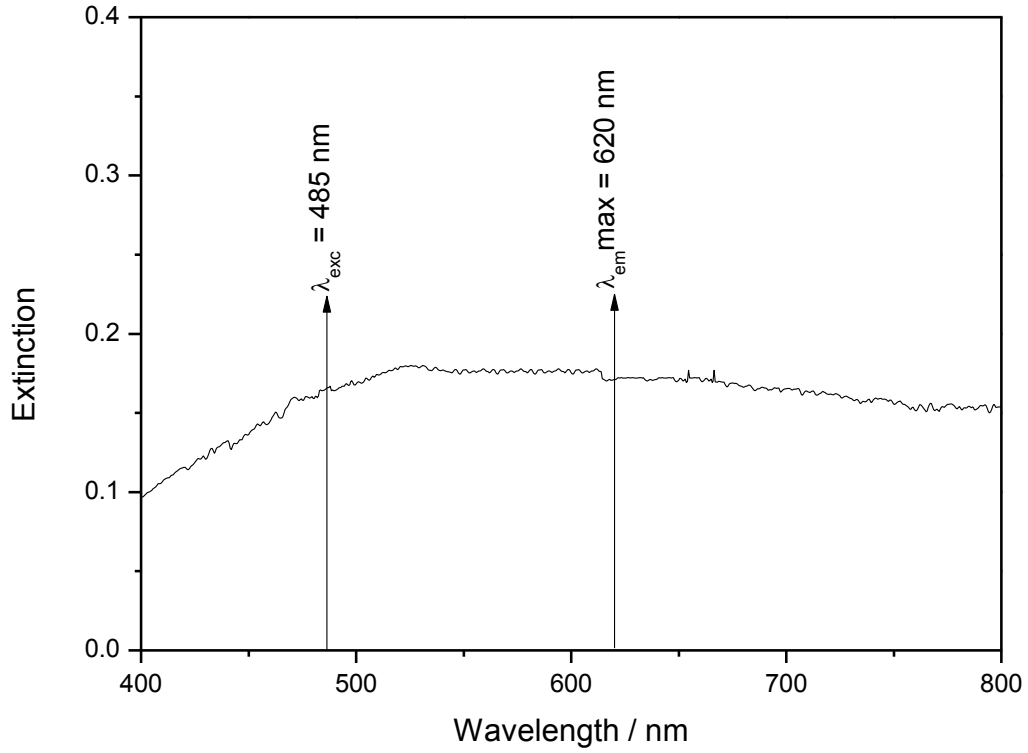

Figure 29: SPE spectra of 3D nanosponge Ag aggregate and projection of excitation and emission maximum wavelengths of $[Ru(bpy)_3]^{2+}$.

5.1.4.2. Phosphorescence lifetime imaging microscopy

The second part of the phosphorescence measurements was focused on exploring how the lifetimes of $[Ru(bpy)_3]^{2+}$ in aqueous solution are affected by the presence of the Ag nanosponge aggregate.

Table 6: Average lifetimes of $[Ru(bpy)_3]^{2+}$ measured from surfaces of Ag nanosponge aggregates and lifetime of $[Ru(bpy)_3]^{2+}$ in the aqueous solution

	τ_1/ns	τ_2/ns	τ_3/ns
1×10^{-5} M $[Ru(bpy)_3]^{2+}$	340	–	–
Ag aggregate overlayed by 1×10^{-5} M $[Ru(bpy)_3]^{2+}$	367	75	17

As is shown in Tab. 6, the lifetime (τ) of free $[Ru(bpy)_3]^{2+}$ ^{3}MLCT excited state is 340 ns. On the other hand, in case of measurement from $[Ru(bpy)_3]^{2+}$ aqueous solution overlayed over Ag aggregate, 3 lifetime values were obtained. The τ = 367 ns respond with the lifetime of free $[Ru(bpy)_3]^{2+}$. Other two shorter lifetimes respond to lifetimes of $[Ru(bpy)_3]^{2+}$ cations which are localized in the vicinity of the aggregate surface or in the aggregate pores. Shortening of lifetime to 75 ns probably corresponds with the localization of $[Ru(bpy)_3]^{2+}$ cations close to the Ag aggregate surface. The other shortening of lifetime to 17 ns is probably related to the localization of molecules of $[Ru(bpy)_3]^{2+}$ into the pores in the Ag aggregate.

The aggregates, in which molecules of $[Ru(bpy)_3]^{2+}$ are incorporated into the internal structure, were also tested. In that case, no phosphorescence signal was observed. It is probably caused by quenching of phosphorescence of $[Ru(bpy)_3]^{2+}$ cations localized in a close vicinity (ca 0.5 nm [23]) from Ag nanostructured surface.

Fig 30 and 31 demonstrate the PLIM images, which were obtained from Ag nanosponge aggregate overlayed by a thin layer of 1×10^{-5} M $[Ru(bpy)_3]^{2+}$, and from which the lifetimes provided in Tab. 6 were determined.

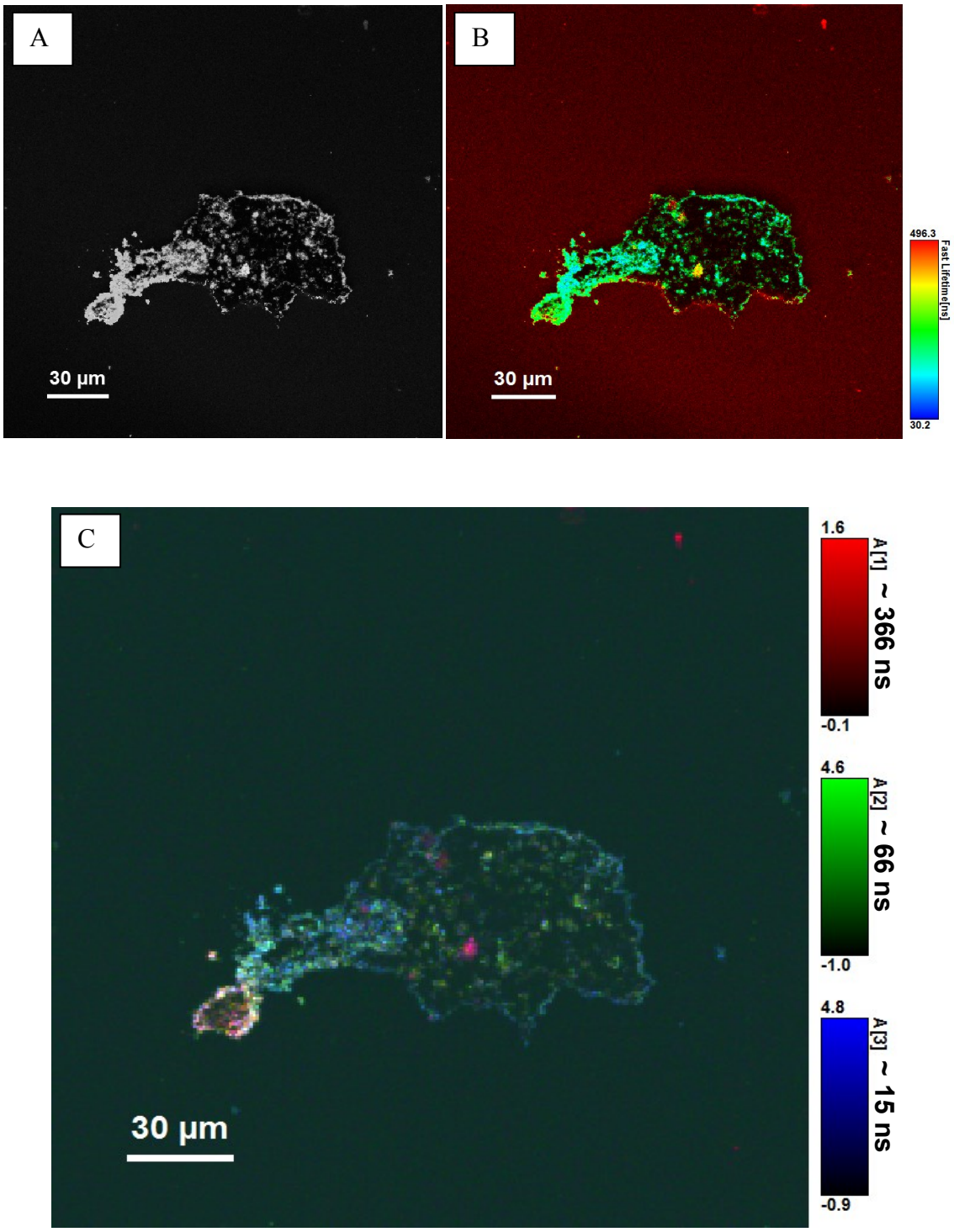

Figure 30: (A) Optical image of Ag nanosponge aggregate (B) PLIM image of Ag nanosponge aggregate with lifetime scale (C) PLIM image of Ag nanosponge aggregate with amplitude scale

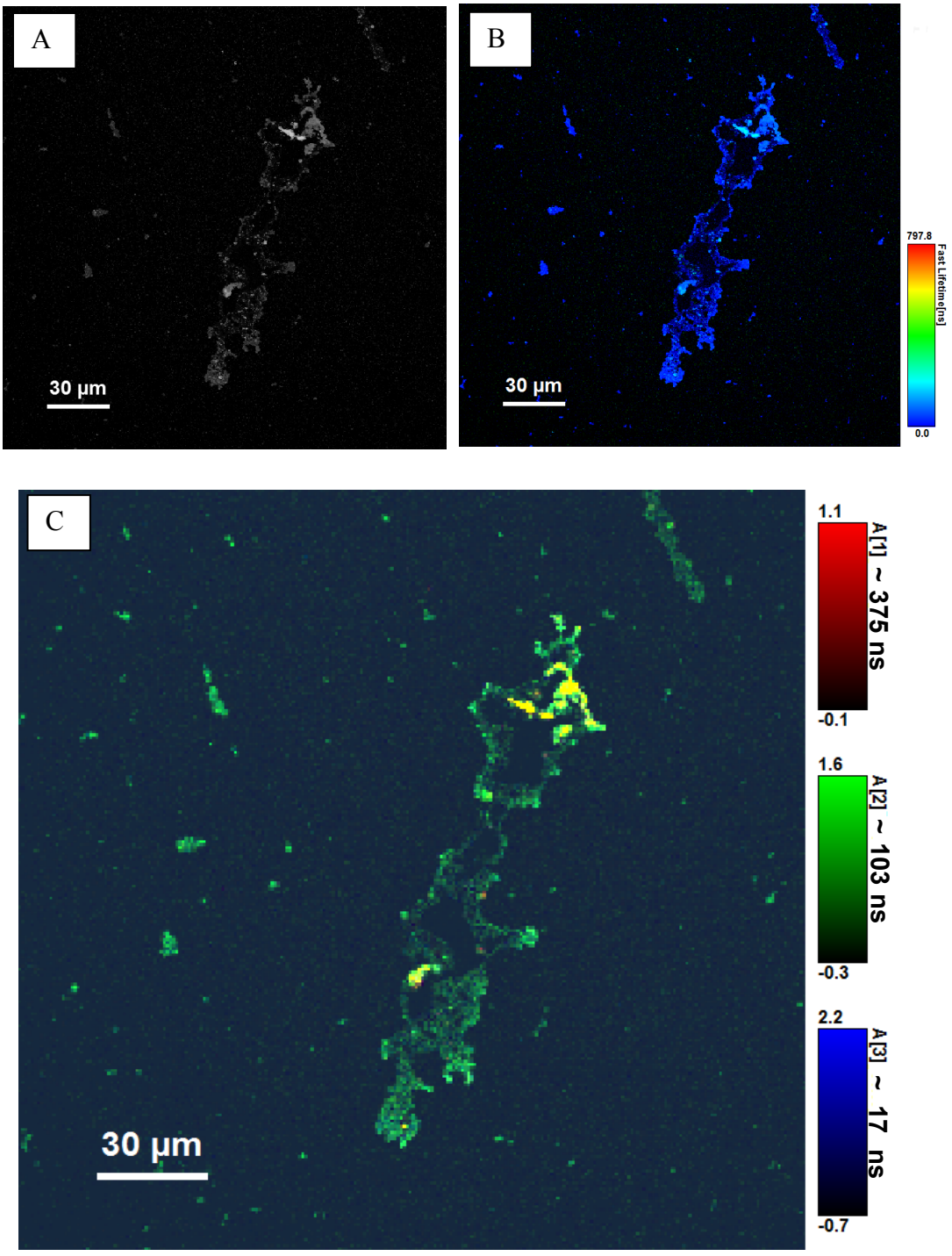

Figure 31: (A) Optical image of Ag nanosponge aggregate (B) PLIM image of Ag nanosponge aggregate with lifetime scale (C) PLIM image of Ag nanosponge aggregate with amplitude scale

5.2. Assembling and co-assembling of hydrophobic Au NPs and semiconductor quantum dots in 2D arrays

5.2.1. Dissolving of hydrophobic Au NPs: preparation and testing of Au NPs organosols

At first, solubility of the commercially obtained hydrophobic Au NPs was handled. For testing of the solubility, toluene, hexane and dichloromethane were used. Several types of solutions were tested. They differ in weight percent of the Au NPs in solution and in the particular solvent. Observation by a naked eye showed that hexane and toluene are suitable solvents for dissolving of Au NPs, while dichloromethane appeared to be a poor solvent. Solubility of Au NPs in organic solvents was further tested by measurements of the UV/vis (i.e. the SPE) spectra. From UV/vis spectra testing of Au NPs, it was shown that hexane and toluene are really suitable solvents for preparation of Au NPs organosols (Fig. 32). Fig. 32 also demonstrates a low solubility of Au NPs in dichloromethane, which is proved by a low value of absorbance (i.e. extinction) of Au NPs (Fig. 32 e – f).

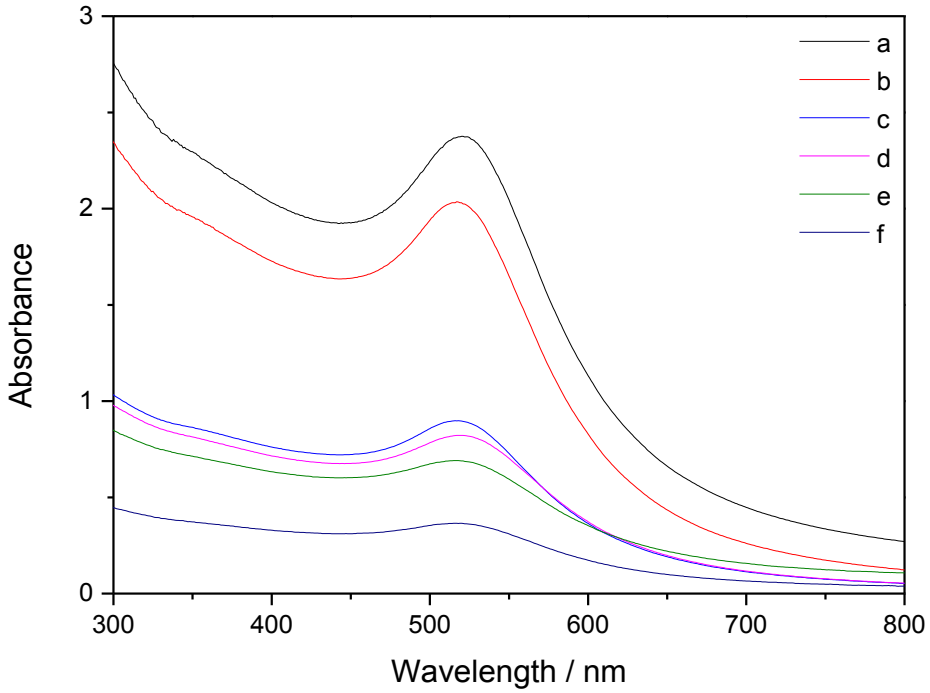

Figure 32: UV/vis (SPE) spectra of organosols of Au NPs with various weight percent amount of Au NPs in various types of solvent: (a) 0.1 % Au in toluene (b) 0.1 % Au in hexane (c) 0.05 % Au in hexane (d) 0.05 % Au in toluene (e) 0.1 % Au in dichloromethane (f) 0.05 % Au in dichloromethane

5.2.2. Assembling of hydrophobic Au NPs

Organosols of hydrophobic Au NPs in the selected organic solvents were deposited onto the microscopic grid and formation of assembled monolayer of Au NPs was followed. Fig. 33 demonstrates that, solutions (organosols) of Au NPs, where the weight percent of Au NPs is 0.1 % are not suitable for preparation of an assembled monolayer, since the Au NPs form clusters or various types of multilayer.

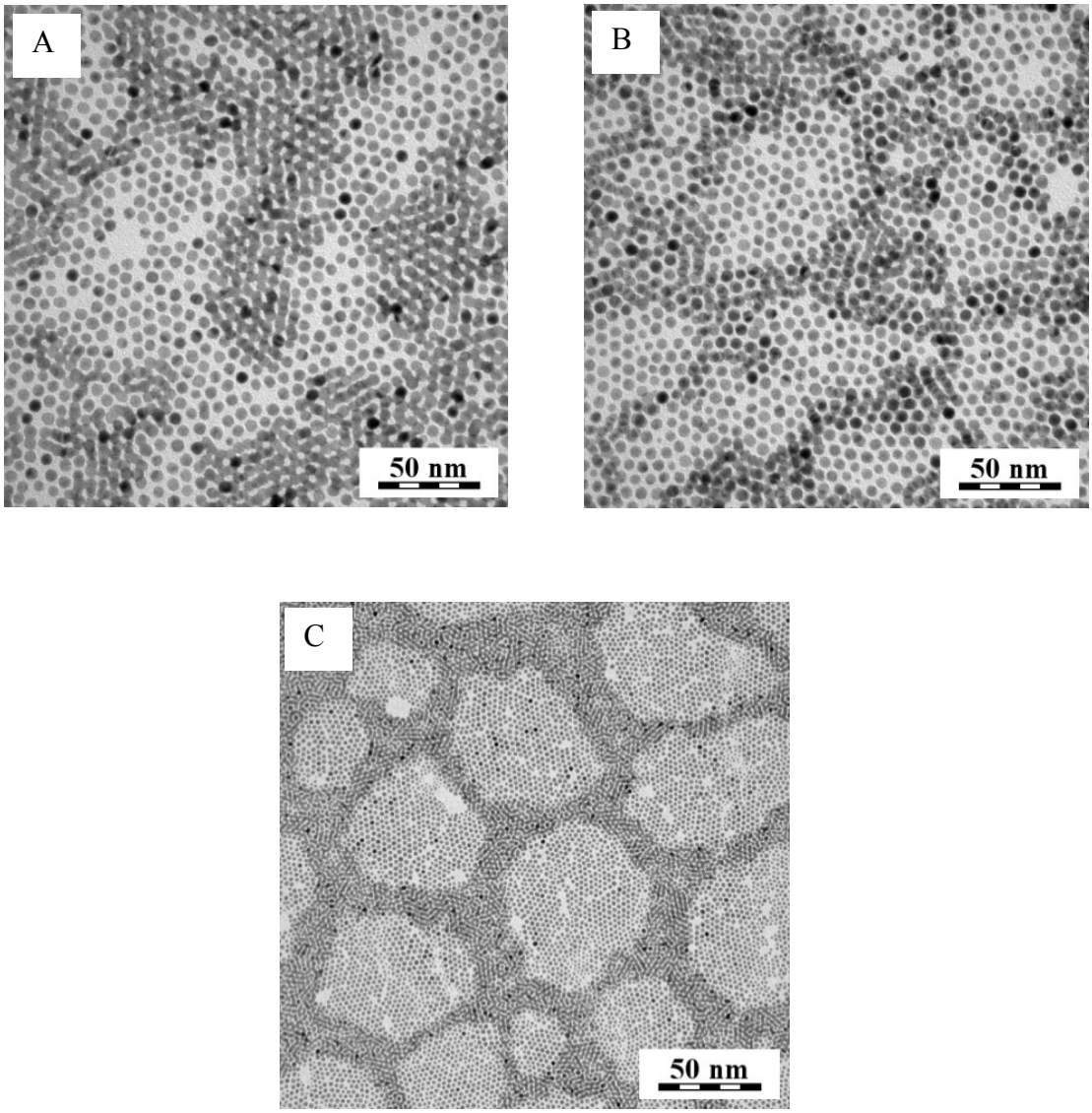

Figure 33: TEM images of Au NPs assembled from organosols (0,01 %) in (A) toluene (B) hexane (C) dichloromethane

Furthermore, the solutions (organosols) of Au NPs, where the weight percent of Au NPs is 0.05 % were tested (Fig. 34). Fig. 34 – A demonstrates that at this concentration, Au NPs in toluene form a 2D assembled monolayer after deposition on carbon – coated TEM grid.

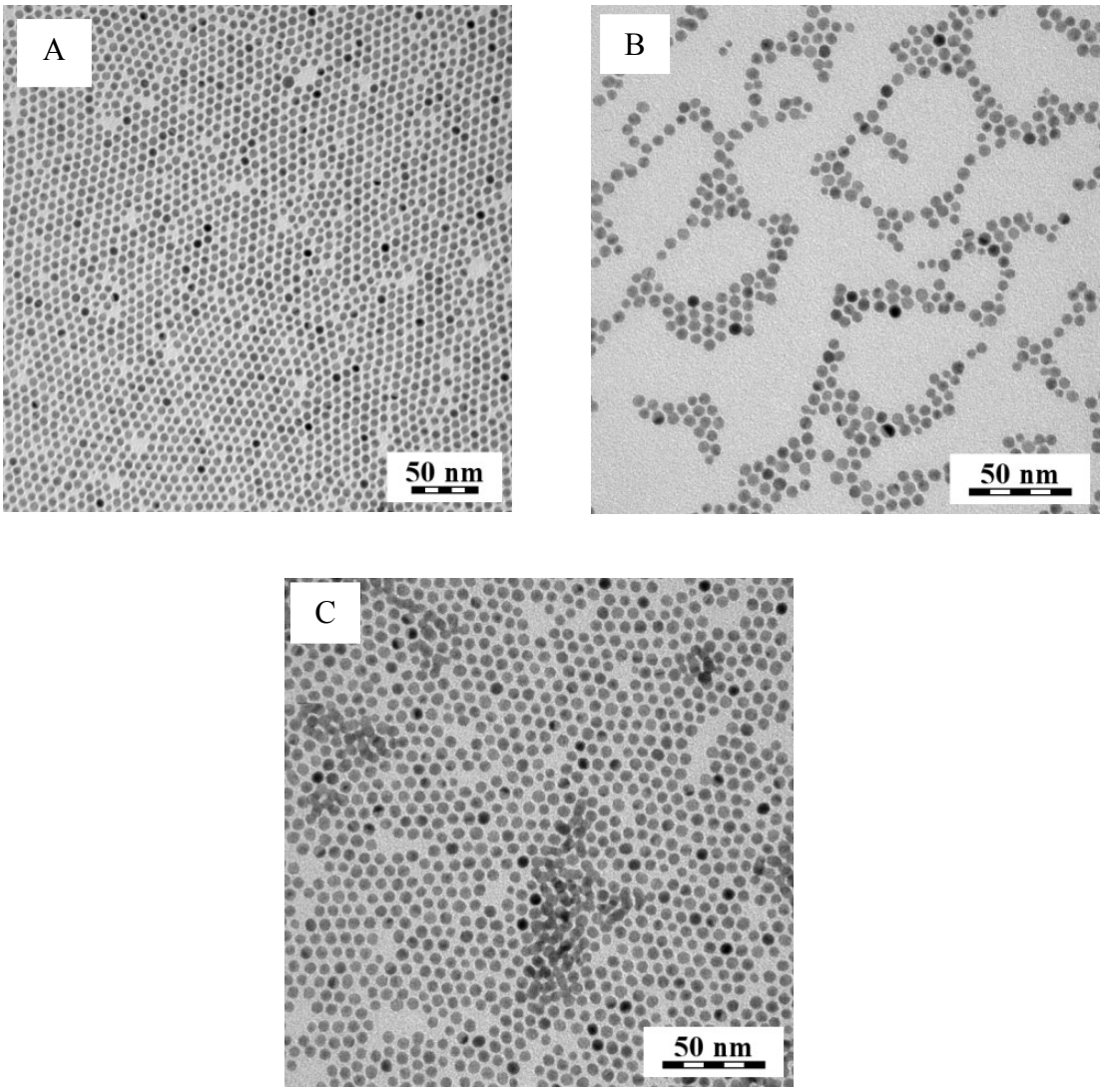

Figure 34: TEM images of 0.05 % Au NPs in (A) toluene (B) hexane (C) dichloromethane

5.2.3. Assembling of hydrophobic SQDs

On the basis of the study of Au NPs assembling, toluene was selected as a perspective solvent for assembling of commercial hydrophobic SQDs. Two types of solutions (organosols) of SQDs in toluene were prepared – 0.05 % solution of SQDs 470 and 0.05 % solution of SQDs 610. As Fig. 35 demonstrates, both types of SQDs organosols form 2D assembled monolayers after deposition.

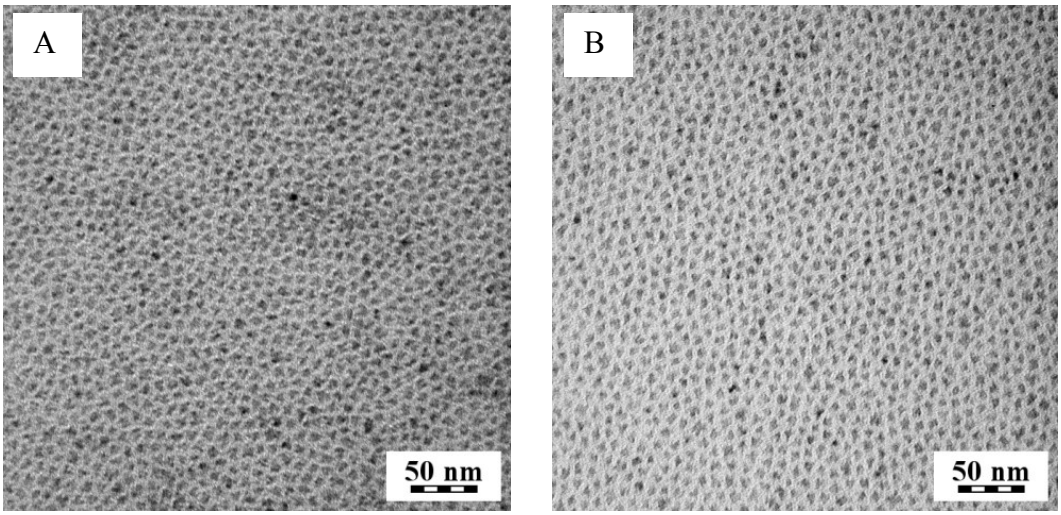

Figure 35: TEM images of SQDs assemblies prepared by deposition of 0.05 % solution of SQDs in toluene (A) SQDs 470 (B) SQDs 610

5.2.4. Co-assembling of hydrophobic Au NPs and semiconductor quantum dots – morphological studies

5.2.4.1. Interfacial films

TEM images of interfacial films of co-assembled Au NPs and SQDs are shown in Fig. 36. SQDs 610 create an assembled layer, however they mix with Au NPs in a very small amount (Fig. 36 – A). Au NPs also form aggregates or clusters on assembled layer of SQDs as demonstrated Fig. 36 – B.

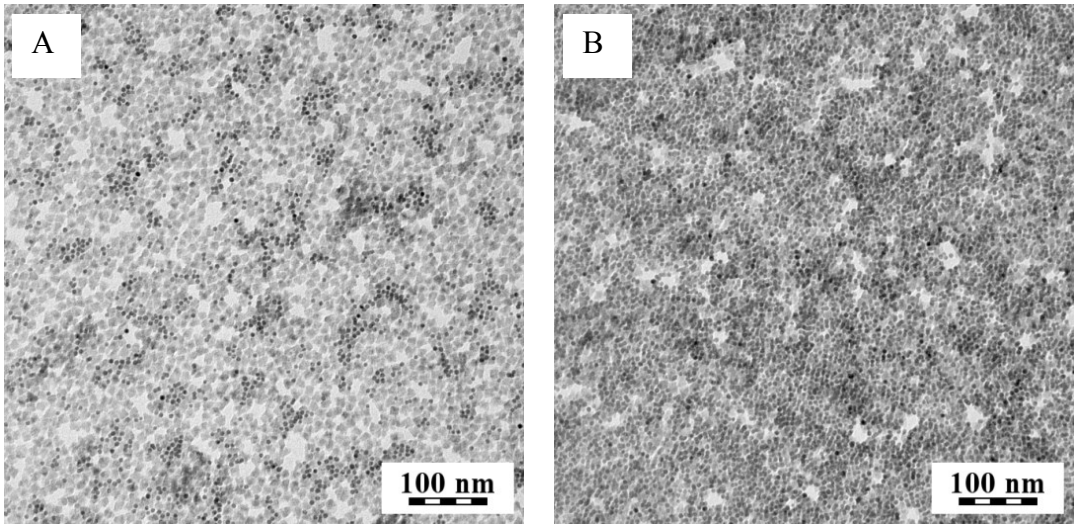

Figure 36: TEM images of interphase films of co-assembled Au NPs and SQDs – 610.

5.2.4.2. Co-assembling of Au NPs and SQDs at water surface

At first, TEM images of co-assembled Au NPs with SQDs at water phase surface were obtained. Fig. 37 A – E shows co-assembled Au NPs and SQDs in the range 4:1 – 1:4 of ratios. In those ratios, where Au NPs or SQDs are not in a large excess, Au NPs and SQDs are co-assembled into a 2D arrays. Fig. 38 A – B demonstrates, that if either Au NPs or SQDs are in a large excess, then co-assembled 2D arrays are not created, but blocks of assembled Au NPs and SQDs or multilayers of Au NPs covered by SQDs are formed.

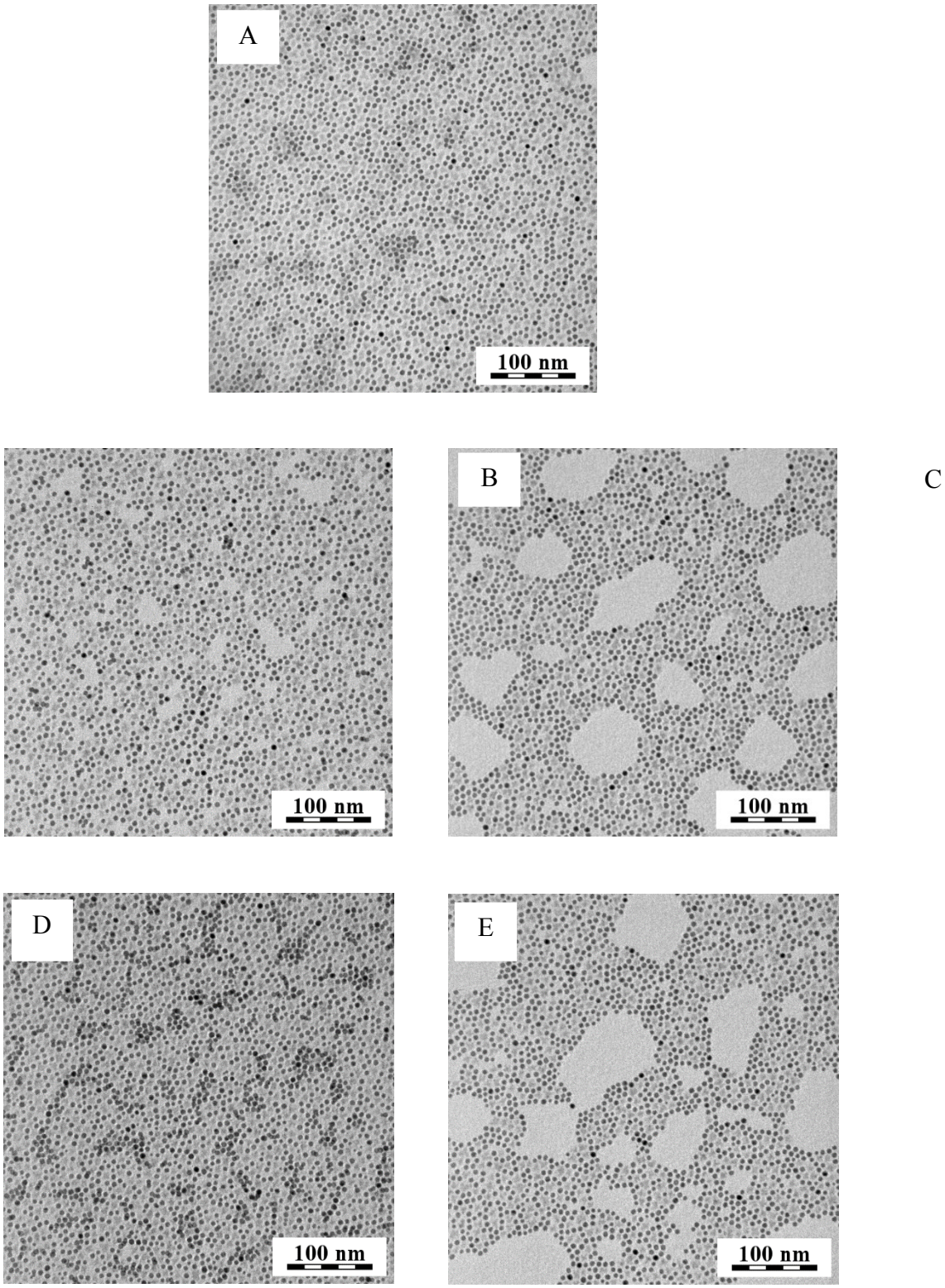

Figure 37: TEM images of co-assembled hydrophobic Au NPs and SQDs in the following ratios 1:1 (A), 1:2 (B), 2:1 (C), 1:4 (D), 4:1 (E)

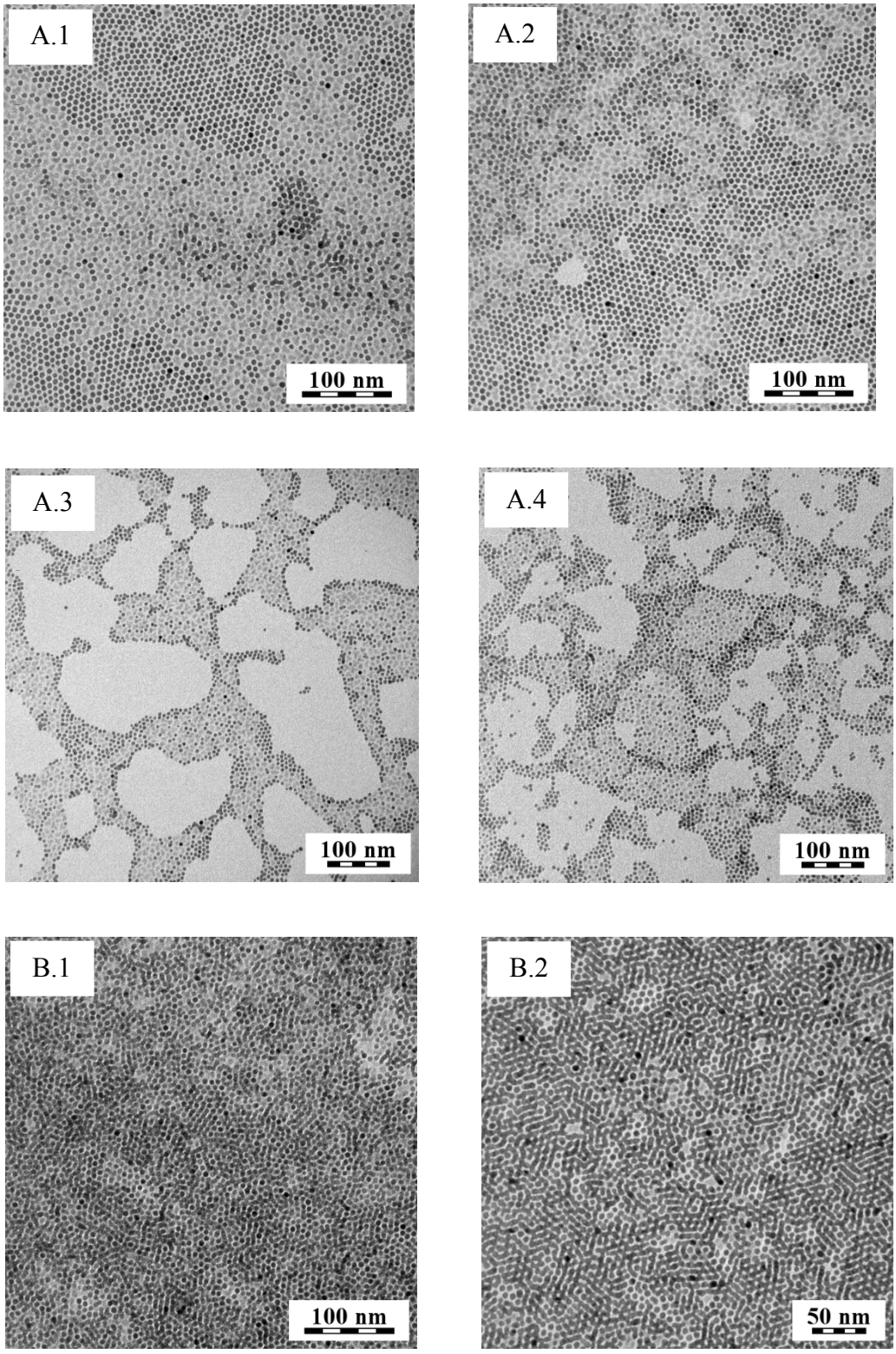

Figure 38: TEM images of co-assembled hydrophobic Au NPs and SQDs in the 1:6 – 1:10 ratios which represent various morphologies of a non-ideal co-assembling (A.1 – 4) blocks of Au NPs and SQDs and partial co-assembling (B.1 – 2) multi layer of Au NPs.

5.2.5. Fluorescence intensity measurements of SQDs co-assembled with Au NPs

First, luminescence (namely fluorescence) of the SQDs from the selected area of the 2-D assembly of SQDs 610 (whose TEM image is depicted in Fig. 35 – B) was measured and it was found to be 17 000 counts (Tables 7 and 8). Subsequently, fluorescence of SQDs from the same selected areas of the AuNPs/SQD co-assemblies with various AuNPs: SQDs weight ratios has been measured, and its intensities are provided in Tab. 7. The largest fluorescence signals (Fig. 39 and Table 7) were obtained from the most regular 2D co-assemblies with a good mutual mixing of AuNPs and SQDs (Fig. 37 – A,B,C). For the AuNP/SQDs 2D co-assemblies with the 1:1, 1:2 and 2:1 AuNPs:SQDs weight ratios, the average values of numbers of both Au NPs and SQDs, and the fractions of SQDs (in % of the total number of particles) were determined by the image analysis of several TEM images. Their values are listed in Table 2, and details are provided in Supplement II. Furthermore, the fluorescence intensities calculated for the 2D samples with a particular fraction of SQDs (in %) in the case of non-enhanced fluorescence have been compared to the measured fluorescence intensities (Table 8). For all three samples, the measured fluorescence intensities are several times larger than the calculated ones, which indicates enhancement of the SQDs fluorescence in the particular co-assemblies with Au NPs. For each of the samples, the fluorescence enhancement factor E_f was calculated as a ratio of the measured to the calculated fluorescence intensity, and listed in Table 8. Nevertheless, this approach actually allows for an estimate rather than an exact determination of the fluorescence enhancement factor, since a more detailed fluorescence intensity mapping and TEM image analysis (currently in progress) is required for obtaining of the more precise E_f values. On the other hand, it is obvious from the results presented in Table 8 and Fig. 37 that in the semiregular 2D co-assemblies in which AuNPs mix with SQDs without a large scale segregation, the enhancement of the SQDs fluorescence by factors in the 7-8 range has been achieved. Considering the origin of the fluorescence enhancement, it should be noted that the SPE curves of the AuNPs/SQDs assemblies with projections of the excitation wavelength at 532 nm and of the wavelength of the emission maximum at 610 nm of the SQDs fluorescence in Fig. 40 demonstrate the overlap of the SPE of Au NPs with both the excitation (absorption) and the emission of SQDs. Both the excitation and emission of SQDs can thus be enhanced by resonance excitations of dipolar surface

plasmons localized on Au NPs and the resulting dipoles emission, and can thus contribute to the observed fluorescence enhancement.

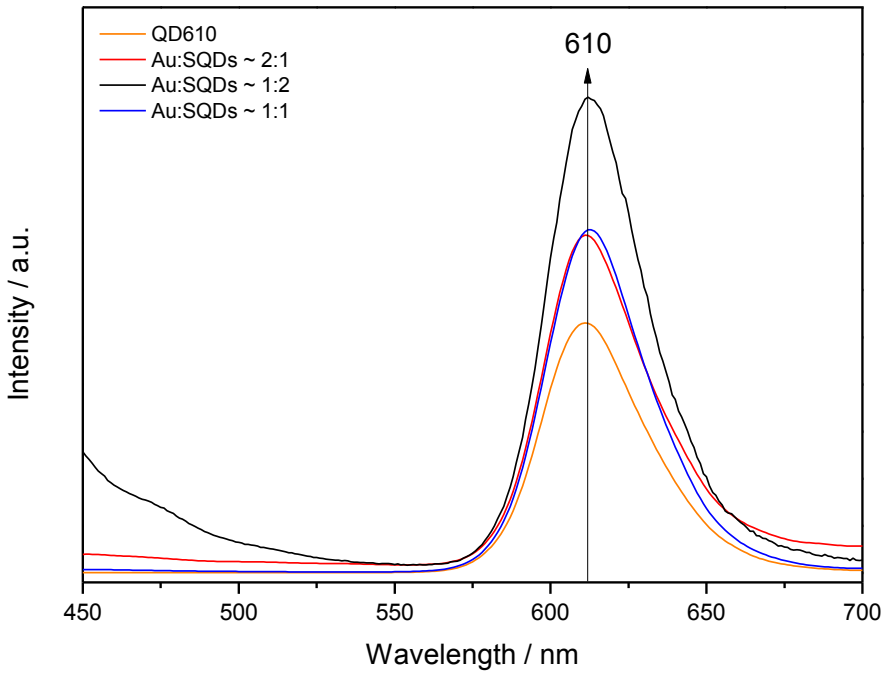

Figure 39: UV-vis spectra of co-assembled hydrophobic Au NPs and SQDs

Table 7: Fluorescence intensities as a function of Au NPs : SQDs weight ratios

Au NPs : SQDs	Intensity
0:1	17 000
1:1	32 000
1:2	57 000
2:1	34 000
1:4	31 000
4:1	15 000
1:6	14 000
6:1	17 000
1:8	14 000
8:1	24 000

1:10	15 000
10:1	13 000

Table 8: Fluorescence intensity of SQDs (100 %) assembly, and the calculated non-enhanced fluorescence intensities, the measured (enhanced) fluorescence intensities and enhancement factor (Ef) of Au NPs : SQDs co-assemblies with a particular of SQDs (in %) of the total number of particles

Au NPs: SQDs weight ratios	% of SQDs	Non-enhanced fluorescence intensity	Measured fluorescence intensity	E_f
0:1	100	17 000	17 000	
1:1	27	4590	32 000	7.4
1:2	42	7140	57 000	6.9
2:1	25	4590	34 000	7.4

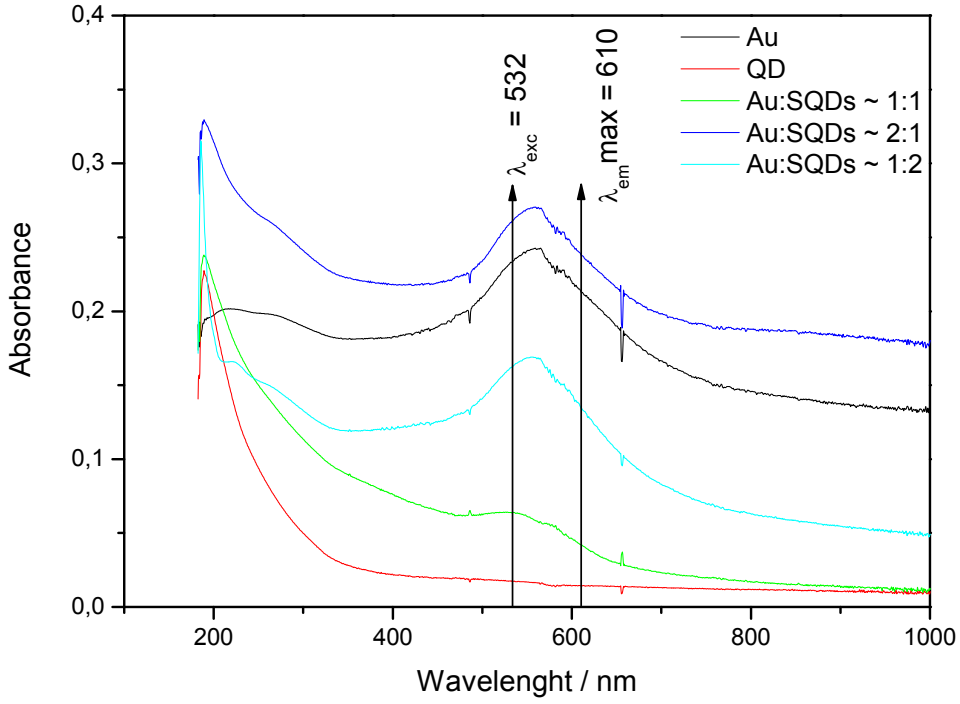

Figure 40: Emission spectra of SQDs and co-assembled Au NPs and SQDs

6. Conclusions

The process of Ag nanosponge aggregates assembling can be tailored for SERS, SERRS and for surface-enhanced luminescence spectral (SEL) measurements of chromophores and luminophores, as demonstrated for $[Ru(bpy)_3]^{2+}$. For SERS and SERRS, the 3D Ag nanosponge aggregates have been assembled from 2D fused fractal aggregates (D = 1.87 ± 0.02) with incorporated chloride anions and $[Ru(bpy)_3]^{2+}$ dications, and overlayed by a thin layer of the aqueous phase. Alternatively, for surface enhanced luminescence, the 3D Ag nanosponge aggregates have been assembled from fused fractal aggregates of chloride-modified Ag NPs and overlayed by a 1×10^{-5} M aqueous solution of $[Ru(bpy)_3]^{2+}$.

In SERRS and SER(R)S spectral measurement at 445 nm and 532 nm excitations, the SERRS (1×10^{-15}) and SER(R)S (1×10^{-14} M) limits of detection of $[Ru(bpy)_3]^{2+}$ correspond to the single molecule level of detection. Achievement of single molecule level of detection is attributed to (i) large EM mechanism enhancement experienced by $[Ru(bpy)_3]^{2+}$ incorporated in hot shots (ii) efficient localization of "hot spots" in the 3D aggregate to the focus of the laser beam in micro-Raman SER(R)S and SERRS spectral measurements and (iii) to molecular resonance contribution to the overall enhancement. Another advantage of SERS, SER(R)S and SERRS spectral measurements from the 3D Ag nanosponge aggregate is protection of the analyte (i.e. $[Ru(bpy)_3]^{2+}$) against thermal decomposition by the thin aqueous phase overlayed.

Phosphorescence measurement of $[Ru(bpy)_3]^{2+}$ from 3D nanosponge aggregate overlayed by 1×10^{-5} M $[Ru(bpy)_3]^{2+}$ aqueous solution have shown enhancement of fluorescence intensity by the factor of 70. From the PLIM studies, three different ^{3}MLCT excited state lifetimes of $[Ru(bpy)_3]^{2+}$ were obtained: 367 ns, 75 ns and 17 ns. The 367 ns lifetime belongs to free $[Ru(bpy)_3]^{2+}$. The other two lifetimes are attributed to $[Ru(bpy)_3]^{2+}$ cations localized in the vicinity of the aggregate or in the aggregate pores, respectively.

The advantage of the newly prepared 3D Ag nanosponge aggregate common to its utilization both as a sample for SERS and SERRS of incorporated adsorbates and as an active surface for SEL of luminophores is its broad SPE, which spans the overall visible spectral region. This allowed to measure SERS and SERRS spectra as a function of

various excitation wavelengths in the overall visible spectral region, as demonstrated in this Thesis for $[Ru(bpy)_3]^{2+}$.

In SEL of $[Ru(bpy)_3]^{2+}$, it enabled to achieve the overlap between the SPE and both the phosphorescence excitation and emission. Utilization of the 3D aggregate for SERRS of a variety of chromophores and SEL of various luminophores can thus be envisaged.

Hydrophobic Au NPs and alloyed ZnCdSeS SQDs in the form of their organosols in toluene were first assembled separately into 2D arrays, and then co-assembled at water surface in various weight ratios. The 1:1, 1:2 and 2:1 ratios were found to be optimal for semiregular 2D co-assembling of Au NPs and SQDs. In these assemblies, localization of SQDs between Au NPs led to enhancement of the SQDs fluorescence by the factor of 7 – 8.

The successful co-assembling of the commercially available hydrophobic Au NPs (6 – 7 nm diameter) and SQDs (~ 6 nm in diameter) in the above mentioned weight ratios is attributed to the similarity of their sizes as well as to their chemical functionalization by hydrophobic species. The observed 7 – 8× enhancement of SQDs fluorescence in the co-assembly with Au NPs is attributed to the overlap between SPE of Au NPs within the assembly with both the SQDs fluorescence excitation and emission, as well as to the particular internal morphology of the assembly.

References

[1] Le Ru, E.C.; Etchegoin, P.G. *Principles of Surface-enhanced Raman Spectroscopy and Related Plasmonic Effects*, Elsevier, Elsevier: Amsterdam, The Netherlands, 2009.

[2] Aroca, R. *Surface-Enhanced Vibrational Spectroscopy,* John Wiley & Sons, Ltd.: , Chichester, U.K., 2006.

[3] Kneipp, K.; Moskovits, M.; a Kneipp, H. *Surface-Enhanced Raman Scattering. Physics and Applications.*, Topics in Applied Physics, *103,* Springer-Verlag: Berlin, Heidelberg, 2006.

[4] Schlucker, S., Ed. *Surface Enhanced Raman Spectroscopy. Analytical, Biophysical and Life Science Applications*, Wiley-VCH: Weinheim, Germany, 2011.

[5] Moskovits, M. *Rev. Mod. Phys*. **1985**, *57*, 783 – 826.

[6] Cialla, D.; Marz, A.; Bohme, R.; Theil, F.; Weber, K.; Schmitt, M.; Popp, J. *Anal. Bioanal. Chem.* **2012,** *403*, 27 – 54.

[7] Le Ru, E.C.; Etchegoin, P.G. *Ann. Rev. Phys. Chem*. **2012**, *63*, 65 – 87.

[8] P. Matějka, B. Vlčková, L. Bednárová, P. Maloň: Advances and Challenges in Optical Molecular Spectroscopy Including Surface Plasmon Resonance-Based Methods for Bioanalysis, in *Natural Products Analysis: Instrumentation, Methods and Applications,* V. Havlíček and J. Spížek, Eds., John Wiley and Sons, Hoboken, New Yersey, USA, 2014.

[9] Geddes, D.Ch Metal-Enhanced Fluorescence, John Wiley & Sons, Inc., Hoboken, New Yersey, 2010.

[10] Lakowicz, J.R.; Principle of Fluorescence Spectroscopy, Third edition, Springer Science + Businnes Media LLC, New York, 2006

[11] Mallick, K.P.; Danzer, D.G.; Strommen, P.D.; Kincaid, R.J. *J. Phys. Chem*. **1998**, *92*, 5628 – 5634.

[12] Kalyanasundaram, K. Photochemistry of Polypyridine and Porphyrin Complexed; Academic Press inc., London, 1992.

[13] Petryayeva, E.; Algar, W.R.; Medintz, L.I. Applied Spectroscopy **2013**, *67*, 215 – 252.

[14] Kneipp, K.; Wang, Y.; Kneipp, H.; Perelman, L.T.; Itzkan, I.; Dasari, R.R.; Feld, M.S. *Phys. Rev. Lett.* **1997**, *78*, 1667 – 1670.

[15] Xu, H.; Aizpurua, J.; Kall, M.; Apell, P. *Phys. Rev. E* **2000**, *62*, 4318 – 4324.

[16] Johansson, P.; Xu, H; Kall, M. *Phys. Rev. B* **2006**, *72*, 035427-1-035427-16.

[17] Vlckova, B.; Moskovits, M.; Pavel, I; Sladkova, M; Siskova, K.; Slouf , M. *Chem. Phys. Lett.* **2008,** *455*, 131-134.

[18] Sládková, M.; Vlčková, B.; Mojzeš, P. Šlouf, M. *Faraday Discuss*. **2006**, *132*, 121 – 134.

[19] Moskovits, M. *J. Chem. Phys*. **1978**, *69*, 4159 – 4161.

[20] Procházka, M.; Mojzeš, P.; Štěpánek, J.; Vlčková, B.; Turpin, P.Y. *Anal. Chem*. **1997**, *69*, 5103 – 5108.

[21] Šišková, K.; Vlčková, B.; Turpin, P.Y.; Thorel, A.; Procházka, M. *J. Phys. Chem.C* **2011**, *115*, 5404 – 5412.

[22] Šloufová-Srnová, I.; Vlčková, B.; Snoeck, L.T.; Stufkens, J.; Matějka, P. *Inorg.Chem* **2000**, *39*, 3551 – 3559.

[23] Kokošková, M.; Procházka, M.; Šloufová, I.; Vlčková, B. *J. Phys. Chem. C* **2013**, *117*, 1044 – 1052.

[24] Fleischmann, M; Hendra, P.J.; McQuillan, A.J. *Chem. Phys. Lett.* **1974**, *26*, 163 – 166.

[25] Jeanmaire, D.L.; van Duyne, R. *J. Electroanal. Chem.* **1977**, *102*, 87 – 88.

[26] Creighton, J.A.; Chang, R.K.; Furtak, T.E. *Metal Colloids in Surface enhanced Raman Scattering*, Eds, Plenum Press, New York, 1982.

[27] Fornasiero, D.; Grieser, F. *J. Phys. Chem*. **1987**, *87*, 3213 – 3217.

[28] Zhang, P.; Haslett, T.L.; Douketis, C.; Moskovits, M. *Phys. Rev. B.* **1998**, *57*, 15513 – 15518.

[29] Drexhage, K.H. *J. Luminesc.* **1970**, *12*, 693.

[30] Lakowicz, R.J *Anal. Biochem* **2001**, *298*, 1 – 24.

[31] Anger, P.; Bharadwaj, P.; Novotny, L. *Phys. Rew. Lett*. **2006**, *96*, 1 – 4.

[32] Lukomska, J.; Malicka, J.; Grynzynski, I.; Lakowicz, J.R. *J. Flourescenc.* **2004**, *14*, 417 – 423.

[33] Oates, T.W.H.; Shiratori, Y.; Noda, S. *J. Phys. Chem. C* **2009**, *113*, 9588 – 9594.

[34] Geddes, D.Ch.; Lakowicz, R.J. *J. Fluoresc.* **2002**, *12*, 121 – 126.

[35] Lakowicz, R.J.; Shen, Y. D´Auria, S.; Malicka, J.; Fang, J.; Grynczyski, Z.; Gryczynski, I. *Anal. Biochem.* **2002**, *301*, 261 – 277.

[36] Malicka, J.; Gryczynski, I.; Gryczynksi, Z.; Lakowicz, J.R. *Anal. Biochem.* **2003**, *315*, 57 – 66.

[37] Fojtik, A.; Henglein, A. *Ber. Bunsenges. Phys.* Chem **1993**, *97*, 252 – 254.

[38] Creighton, J.A.; Blatchford, C.G.; Albrecht, M.G. J. Chem. Soc. 2, Faraday Trans. **1979**, *75*, 790 – 798.

[39] Laserna, J.J.; Torres, E.L.; WInefordner, J.D. *Anal. Chim. Acta.* **1987**, *200*, 469 – 480.

[40] Heard, S.M.; Grieser, D.P.; Barraclough, C.G. *Chem. Phys. Lett.* **1983**, *95*, 154 – 158.

[41] Stockman, M.I.; Shalaev, V.M.; Moskovits, M.; Botet, R.; Georgie, T.F. *Phys. Rev.* **1992**, 46, 2821.

[42] Šimáková, P.; Procházka, M.; Kočišová, E. *Spectroscopy: An International Journal* **2012**, *27*, 449 – 453.

[43] Kong, L.; Dong, R.; Ma, H.; Hao, J. *Langmuir* **2013**, *29*, 4235 – 4241.

[44] Tang, S.; Vongehr, S.; Wang, Y.; Cui, J.; Wang, X.; Meng, X. *J. Mater. Chem. A* **2014**, *2*, 3648 – 3660.

[45] Marques, P.A.A.P.; Nogueira, I.S.H.; Pinto, J.B.R.; Neto, P.C.; Trindade, T. *J. Raman. Spec.* **2008**, *39*, 439 – 443.

[46] Sutrová, V.; Šloufová, I.; Nevoralová, M.; Vlčková, B. J. Raman. Spec. 2015, DOI 10.1002/jrs. 4690.

[47] Dines, T.; Peacock D.R. *J. Chem. Soc., Faraday Trans. 1* **1998**, *84*, 3445 – 3457.

[48] Forster, M., Hester E.R., *Chem. Phys. Lett*., **1981**, *81*, 42 – 47.

[49] Kulakovich, O.; Strekal, N.; Yaroshevich, A.; Makevich, S.; Gaponenko, S.; Nabiev, I.; Woggon, U.; Artemyev, M.; *Nano Lett.* **2002**, *2*, 1449 – 1452.

[50] Song, J.H; .; Atay, T.; Shi, S.F.; Urabe, H.; Nurmikko, A.V. *Nano Lett.* **2005**, *5*, 1557 – 1561.

[51] Pompa, P.P.; Martiradonna, L.; Della Torre, A.; Carbone, L.; del Marcato, L.L.; Manna, L., De Vittorio, M.; Calabi, F.; Cingolani, R.; Rinaldi, R. *Sensors. Actuat. B-Chem.* **2007**, *126*, 187 – 192.

[52] Leong, K.; Chen, Y.; Masiello, D.J.; Zin, M.T.; Hnilova, M.; Ma, H.; Tamerler, C.; Sarikaya, M.; Ginger, D.S.; Jen, A.K.Y. *Adv. Func. Mater.* **2010**, *20*, 2675 – 2682.

[53] Hafenist, A.S.; Wang. L.Z.; Alvarez, M.M.; Vezmar, I.; Whetten, L.R. *J. Phys. Chem.* **1996**, *100*, 13904 – 13910.

[54] Wang, X.; Zhuang, J.; Peng, Q.; Li, Y. *Nature* **2005**, *437*, 121 – 124.

[55] Solecká-Čermáková, K.; Vlčková, B.; Lednický, F. *J. Phys. Chem*. **1996**, *100*, 4954 – 4960.

[56] Šloufová-Srnová, I.; Vlčková, B. *Nano Letters*, **2002**, *2,* 121-125.

[57] Vlčková, B.; Šmejkal, P.; Michl, M.; Procházka, M.; Mojzeš, P.; Lednický, F. *J. Inorg. Biochem.,* **2000**, *79*, 295-300.

[58] Corricelli, M.; Depalo, N.; Fanizza, E.; Altamura, D.; Giannini, C.; Siliqi, D.; Mundo R.; Palumbo, F.; Kravets, G.V.; Grigorenko, N.A.; Agostiano, A.; Stricolli, M.; Curri, L.M. *J. Phys. Chem. C* **2014**, *118*, 7579 – 7590.

[59] Haldar, K.K.; Sen, T.; Patra, A. *J. Phys. Chem. C* **2010**, *114*, 4869 – 4874.

[60] Tang, Y.; Yang, Q.; Wu, T.; Liu. L.; Ding, Y.; Yu, B.; *Langmuir*, **2014**, *30*, 6324 – 6330.

[61] Leopold, N.; Lendl, B. A. *J. Phys. Chem. B* **2003**, *107*, 5273 – 5727.

[62] Larmour, I.A.; Faulds, K.; Graham, D. *J. Raman Spectrosc.* **2012**, *43*, 202 – 206.

[63] Pfeifer, P. Obert, M. in *The Fractal Approach to Heterogeneous Chemistry,* Avnir, D. (Ed.) John Wiley & Sons, New York, 1989.

[64] Weitz, D.A., Lin, M.Y.; Sandroff, C.J. *Surf. Sci*. **1985**, *158,* 147 – 164.

[65] Siiman O., Feichenfeld H., *J.Phys.Chem,* **1988**, *92*, 453 – 464.

List of abbreviations

$[Ru(bpy)_3]^{2+}$	Tris(bipyridyl) Ru(II) dichloride
SERS	Surface-enhancement Raman scattering
SER(R)S	Surface-enhancement (resonance) Raman scattering
SERRS	Surface-enhancement resonance Raman scattering
NP/ NPs	Nanoparticle/ Nanoparticles
SQDs	Semiconductor quantum dots
EM	Electromagnetic mechanism
MR	Mechanism of molecular resonance
SML	Surface modified luminescence
SEL	Surface-enhanced luminescence
MLCT	Metal to ligand charge transfer
NCA	Normal coordinate analysis
PL	Photoluminescence
H_2TMPyP	5,10,15,20-tetrakis(1-methyl-4-pyridyl)-21H, 23H porphine

Supplement

I. Calculation of number of molecules incorporated into the 3D Ag nanosponge aggregate

Assumption for calculation
I.
The fraction of Ag from the overall amount of Ag in the parent HA-Ag hydrosol system present in the high of 2D fused aggregates is equal to its width determined from the 2D-TEM images, i.e. a cylindrical shape with a diameter (d) is assumed
II.
The laser-beam illuminated area of the aggregate is approximately equal to the fraction of $[Ru(bpy)_3]^{2+}$ dications from the overall amount of $[Ru(bpy)_3]^{2+}$ present in the parent system which is present in the illuminated aggregate area.

Parameters of Ag atoms					
a [A]	ρ [g/cm^3]	Mr	m [g]	V[A3] 1 atom	r [A]
4,0862	10,5	107,9	1,7915E-22	17,05685145	1,596872
	ρ[mg/μm^3]				
	1,05E-08				

HA-Ag NPs hydrosol	
$AgNO_3$	1×10^{-2} (0.0170 g)
Mr($AgNO_3$)	169.87 g/mol
n ($AgNO_3$)	9.999×10^{-5} mol
n (Ag)	9.999×10^{-5}
Total volume of HA-Ag NPs hydrosol	100.3 ml
m Ag in entire HA-Ag NPs hydrosol	10.7887 mg
m Ag in 1 ml of HA-Ag NPs hydrosol	**0.1076 mg**
n Ag in 1 ml of HA-Ag NPs hydrosol	9.97×10^{-7} mol

Blue fields must be entered to calculation

CALCULATION

I.

TEM images of 2D fused aggregates
Surface occupancy from TEM image analysis of 4 images

	0.66
	0.55
	0.65
	0.51
average	**0.6**

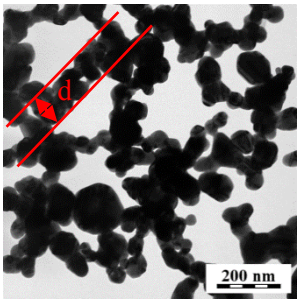

In the area of	**1**	**x**	**1**	**µm²**	Occupied fraction =	**0,6 µm²**
Average diameter of 2D fused aggregates					70	nm

II.

60% occupied area, i.e. 0.6 µm width from 1 µm

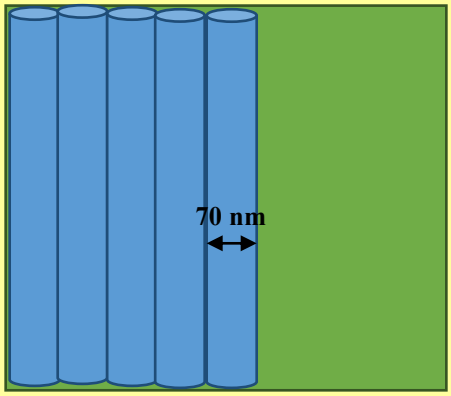

1 µm

1 µm

70 nm = diameter of cylinder

III.

Volume of the cubic illuminated area	1×1×1	μm^3
The total volume of the layer	0.07	μm^3
The volume occupied by a cylinder of 70 nm diameter	0.003848	μm^3
Number of cylinders with a diameter of 70 nm per occupied area (0.6 fraction)	8.5	
The volume occupied by the cylinders in 1 layer	0.032574	μm^3
The total number of 70 nm layers in the cube	14.3	
The total occupied volume in the cube	0.465348	μm^3
Fraction of the ocupied volume	0.47	
Amount of Ag in the cube	4.89×10^{-9}	mg

The fraction of the overall amount of Ag in 2 mL of HA-Ag NPs hydrosol present in the illuminated volume	**2.3×10^{-8}**

IV.		
Concentration of $[Ru(bpy)_3]^{2+}$ in solution	1×10^{-14}	M
Volume of HA-Ag NPs hydrosol/HCl/$[Ru(bpy)_3]^{2+}$	2	ml
Number of $[Ru(bpy)_3]^{2+}$ cations in the system	1.2×10^{7}	
Fraction of $[Ru(bpy)_3]^{2+}$ in the laser illuminated volume of the aggregate	2.3×10^{-8}	
Number of $[Ru(bpy)_3]^{2+}$ cations in the laser illuminated volume of the aggregate	$2.8\times10^{-1} \sim 0.3$	cations

II. TEM images image analysis

1	Creation of Binary image from Au NPs which has got higher contrast than SQDs and determination of number of Au NPs in measure frame • analysis were done from only from measure frame, which was the same for all analysis	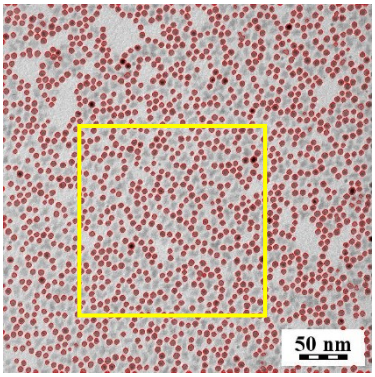
2	Creation of Binary image from all particles at TEM imate and determination of thet total number of particles • analysis were done from only from measure frame, which was the same for all analysis	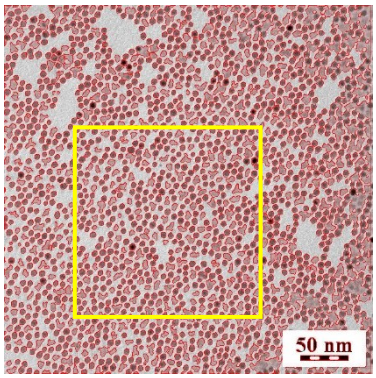
3	Calculation of number of SQDs	All particles – Au NPs